

1 **GUST1.0: A GPU-accelerated 3D Urban Surface Temperature Model**

2 Shuo-Jun Mei^{1,2*}, Guanwen Chen^{1,2}, Jian Hang^{1,2}, Ting Sun³

3 ¹ School of Atmospheric Sciences, Sun Yat-sen University, and Southern Marine Science and
4 Engineering Guangdong Laboratory (Zhuhai), Zhuhai 519082, PR China

5 ² China Meteorological Administration Xiong'an Atmospheric Boundary Layer Key Laboratory,
6 Xiong'an, P.R. China

7 ³ Department of Risk and Disaster Reduction, University College London, London, UK

8 *Correspondence to:* Shuo-Jun Mei (meishj@mail.sysu.edu.cn)

9 **Abstract**

10 The escalating urban heat, driven by climate change and urbanization, poses significant threats to
11 residents' health and urban climate resilience. The coupled radiative-convective-conductive heat transfer
12 across complex urban geometries makes it challenging to identify the primary causes of urban heat and
13 develop mitigation strategies. To address this challenge, we develop a GPU-accelerated Urban Surface
14 Temperature model (GUST) through CUDA architecture. To simulate the complex radiative exchanges
15 and coupled heat transfer processes, we adopt Monte Carlo method, leveraging GPUs to overcome its
16 computational intensity while retaining its high accuracy. Radiative exchanges are resolved using a
17 reverse ray tracing algorithm, while the conduction-radiation-convection mechanism is addressed
18 through a random walking algorithm. The validation is carried out using the Scaled Outdoor
19 Measurement of Urban Climate and Health (SOMUCH) experiment, which features a wide range of
20 urban densities and offers high spatial and temporal resolution. This model exhibits notable accuracy in
21 simulating urban surface temperatures and their temporal variations across different building densities.
22 Analysis of the surface energy balance reveals that longwave radiative exchanges between urban surfaces
23 significantly influence model accuracy, whereas convective heat transfer has a lesser impact. To
24 demonstrate the applicability of GUST, it is employed to model transient surface temperature
25 distributions at complex geometries on a neighborhood scale. Leveraging the high computational
26 efficiency of GPU, the simulation traces 10^5 rays across 2.3×10^4 surface elements in each time step,
27 ensuring both accuracy and high-resolution results for urban surface temperature modeling.

28 1. Introduction

29 Urban overheating has become a pressing issue due to the combination effects of global warming,
30 heatwaves, and rapid urbanization ([Feng et al., 2023](#)). The Urban Heat Island (UHI) effect is
31 characterized by higher surface and air temperatures in urban areas than in surrounding rural areas, which
32 exacerbates the urban overheating ([Manoli et al., 2019](#)). It is estimated that more than 1.7 billion people
33 and 13,000 cities are facing urban overheating problems ([Tuholske et al., 2021](#)). Exposure to extreme
34 urban heat poses a significant threat to residents' health, contributing to increased mortality and morbidity
35 ([Ebi et al., 2021](#)).

36 To tackle urban overheating, a precise understanding of the factors driving excessive surface heat is
37 essential, making accurate modeling of urban surface temperatures a critical step toward developing
38 effective mitigation strategies. Urban surface temperatures are commonly simulated with urban land
39 surface schemes (LSMs). To capture the complex exchanges of energy and momentum within an urban
40 environment, these schemes range from simplified approaches that represent the city as a single
41 impervious slab to advanced frameworks that explicitly incorporate the three-dimensional geometry of
42 buildings with varying heights and material properties. The Urban-PLUMBER project has evaluated 32
43 such schemes ([Grimmond et al., 2010](#); [Grimmond et al., 2011](#)), and classified them into ten categories
44 based on the level of three-dimensional detail represented. The most detailed of these are the building-
45 resolved schemes, which explicitly solve airflow and heat transfer while representing the full three-
46 dimensional urban landscape.

47 Building-resolved models, such as VTUF ([Nice, 2016](#)) and computational fluid dynamics (CFD) tools
48 ([Carmeliet and Derome, 2024](#)), solve the governing physical processes at high spatial and temporal
49 resolution. These models are powerful tools for examining the urban thermal balance and identifying the
50 primary drivers of urban heat ([Carmeliet and Derome, 2024](#)). They enable a quantitative evaluation of
51 the contribution of each process, such as conduction, radiation, and convection, to the overall thermal
52 balance. This is particularly important for Asian cities, which are characterized by high-density, high-
53 rise developments and complex urban geometry. Findings from the Scaled Outdoor Measurement of
54 Urban Climate and Health (SOMUCH) project highlight the intricate influence of building morphology

55 on the thermal environment, especially under super-high-density conditions ([Hang and Chen, 2022](#)).
56 These effects arise from complex three-dimensional urban landscapes, including irregular building forms
57 and intricate shading patterns. Accordingly, models representing high-density Asian cities need greater
58 accuracy and flexibility to account for these features.

59 Building-resolved urban surface temperatures are determined by the coupled heat transfer processes of
60 conduction, radiation, and convection ([Krayenhoff and Voogt, 2007](#)). These heat transfer processes in
61 urban areas differ from those in rural areas. First, urban materials typically have a lower heat capacity,
62 allowing them to heat up more quickly and reach higher temperatures ([Wang et al., 2018](#)). Secondly, [the complex three-dimensional geometry of urban environments leads to multiple reflections, which enhance the absorption of solar radiation by surfaces and reduce the net reflected radiation escaping to the atmosphere](#)
63 [the complex three-dimensional geometry of urban environments leads to multiple reflections,](#)
64 [which reduce reflected solar radiation and limit the longwave heat loss to sky](#) ([Yang and Li, 2015](#)).
65 Thirdly, the densely packed buildings weaken the urban wind and thus reduce the convective transfer
66 and further limit the heat loss ([Wang et al., 2021](#)).

69 A well-designed building-resolved model needs to accurately capture these heat transfer processes. Table
70 1 summarizes the models for urban surface temperatures and their schemes for conduction, radiation,
71 and convection. For heat conduction, 1D models are commonly used due to the relatively thin walls of
72 buildings in urban areas. For convective heat transfer, both parameterized convective coefficients and
73 CFD simulations are commonly used. CFD simulations can better capture the spatial variations in air
74 temperature in densely built urban areas, but the computational cost is much higher.

75 The key distinction among these models lies in their radiation schemes, as radiation is the primary energy
76 input into the thermal system of urban surfaces. Moreover, simulating complex urban radiative transfer
77 requires significant computational resources, necessitating simplifications and parameterizations to make
78 the simulation more applicable. For the radiative exchange between urban surfaces, the radiosity method
79 is widely adopted. This approach first collects luminous energy from direct solar and diffuse sky sources
80 and then redistributes reflected energy according to view factors, which quantify the geometric
81 relationships among surfaces. View factors can be determined analytically for simple geometries,

82 estimated with the discrete transfer method (hemisphere discretization and ray counting), or calculated
83 using Monte Carlo ray tracing (MCRT). However, the radiosity method assumes purely diffuse
84 reflections and depends on precise view-factor calculations, making it less accurate for complex urban
85 geometries and surfaces containing semi-transparent materials.

86 In contrast, the MCRT approach offers greater flexibility and has been widely employed to model solar
87 radiation on complex urban surfaces ([Kondo et al., 2001](#)). More recently, its use has expanded beyond
88 radiative transfer to encompass coupled conduction, convection, and radiation processes ([Villefranque et
89 al., 2022](#)). In backward MCRT, the energy of the incident light is divided into a large number of photons.
90 By tracking the path of these photons and counting the number of photons absorbed, the net solar
91 radiation reaching a given surface can be calculated. For example, the HTRDR-Urban adopted the
92 backward MCRT, to calculate the solar radiation considering multiple reflections ([Schoetter et al., 2023](#)).
93 Building on this concept, [Tregan et al. \(2023\)](#) proposed a theoretical framework to solve linearized
94 transient conduction-radiation problems with Robin's boundary condition in complex 3D urban geometry.
95 Based on that framework, [Caliot et al. \(2024\)](#) developed a probabilistic model to simulate urban surface
96 temperatures, using ray-tracing, walk-on-sphere and double randomization techniques. Their model
97 leverages advancements in computer graphics for image synthesis and the MCM, enabling it to
98 effectively handle large and complex 3D geometries.

99 The MCRT method has demonstrated strong capability for accurately modeling coupled heat and
100 radiation processes in complex urban environments, but its high computational cost and low efficiency
101 currently limit its application to real-world urban configurations. Although several models listed in Table
102 1 have been validated against field measurements, others remain unverified and rely on various
103 assumptions and parameterizations, which reduces confidence in their accuracy. Furthermore, the use of
104 field measurement data for model validation faces persistent challenges: 1) limited test points due to
105 regulatory constraints and installation difficulties, 2) uncertainty in infrared imagery caused by varying
106 view angles, and 3) heterogeneity in the optical and thermal properties of building materials.

107 This study aims to develop a GPU-accelerated Urban Surface Temperature (GUST) model to enhance
108 the computational speed of Monte Carlo Method. The model is designed to operate at the neighborhood

109 scale and to capture microscale processes, including complex shading patterns, multiple reflections of
110 solar radiation, and longwave radiative exchanges between building surfaces and the ground. The
111 ultimate objective is to identify the physical drivers of extreme heat in high-density urban neighborhoods.
112 The absorption and reflection of longwave and solar radiation on outdoor surfaces modeled using the
113 reverse Monte Carlo ray tracing (rMCRT) algorithm. The resulting solar and longwave radiation are then
114 treated as heat flux boundary conditions for the 1D heat conduction model, which employs the Monte
115 Carlo random walk method to calculate surface temperatures. High spatial-temporal resolution surface
116 temperature data from a scaled measurement (SOMUCH) is employed to validate the parameterization
117 and assumptions in this model.

118 The paper is organized as follows. Sect. 2 outlines the model structure and describes the algorithms used
119 for the submodels. Sect. 3 presents the validation and evaluation of the model by comparing it with
120 experimental data. Sect. 4 includes an example demonstrating how the model can be applied to complex
121 geometries. Sect. 5 discusses the applications, limitations, and future development of the model. Lastly,
122 Sect. 6 provides the conclusions.

123

124 **Table 1.** Overview of building-resolved models for urban surface temperature. The view factors are
125 solved by both DTM (Discrete transfer method), analytical model, and Monte Carlo ray tracing method.

| Model | Solar | Reflections and Conduction | Convection | Validation | |
|---|----------------------------------|---|-----------------------------|-------------------------|---|
| | Irradiation | longwave exchange | | | |
| HTRDR-Urban (Schoetter et al., 2023) | Backward Monte Carlo ray tracing | Backward Monte Carlo ray tracing | Monte Carlo random walking | Parameterized N.A. | |
| MUST (Yang and Li, 2013) | Sunlit-shaded distributions | Radiosity Method, DTM view factors | 1D heat conduction | Parameterized | Thermal scanner and IRT (Voogt and Oke, 1998) |
| TUF-3D (Krayenhoff and Voogt, 2007) | Sunlit-shaded distributions | Radiosity Method, analytical view factors | 1D heat conduction | Parameterized | Thermal scanner and IRT (Voogt and Oke, 1998) |
| SOLENE Microclimat (Imbert et al., 2018) | Sunlit-shaded distributions. | Radiosity Method, analytical view factors | 1D heat conduction | Coupling CFD simulation | Thermographies measurement (Hénon et al., 2012) |
| Envi-Met (Eingrüber et al., 2024) | Flux reduction coefficients | Radiosity Method, DTM view factors | 1D heat conduction | Coupling CFD simulation | Field measurements (Forouzandeh, 2021) |
| uDALES (Owens et al., 2024) | Sunlit-shaded distributions | Radiosity Method, DTM view factors | 1D heat conduction | Coupling CFD simulation | N.A. |
| PALM (Resler et al., 2017) | Sunlit-shaded distributions | Radiosity Method, Analytical and DTM view factors | Empirical heat conductivity | Coupling CFD simulation | Field measurement (Resler et al., 2017) |
| MITRAS (Salim et al., 2018) | Meso-scale radiation scheme | Meso-scale radiation scheme (METRAS) | Force-restore method | Coupling CFD simulation | N.A. |
| OpenFOAM (Rodriguez et al., 2024) | Sunlit-shaded distributions | Radiosity Method, DTM view factor | 1D heat-moisture diffusion. | Coupling CFD simulation | N.A. |
| FLUENT (Topalar et al., 2015) | Sunlit-shaded distributions | Radiosity Method, DTM view factor | Shell conduction | Coupling CFD simulation | Field measurement (Topalar et al., 2015) |

126

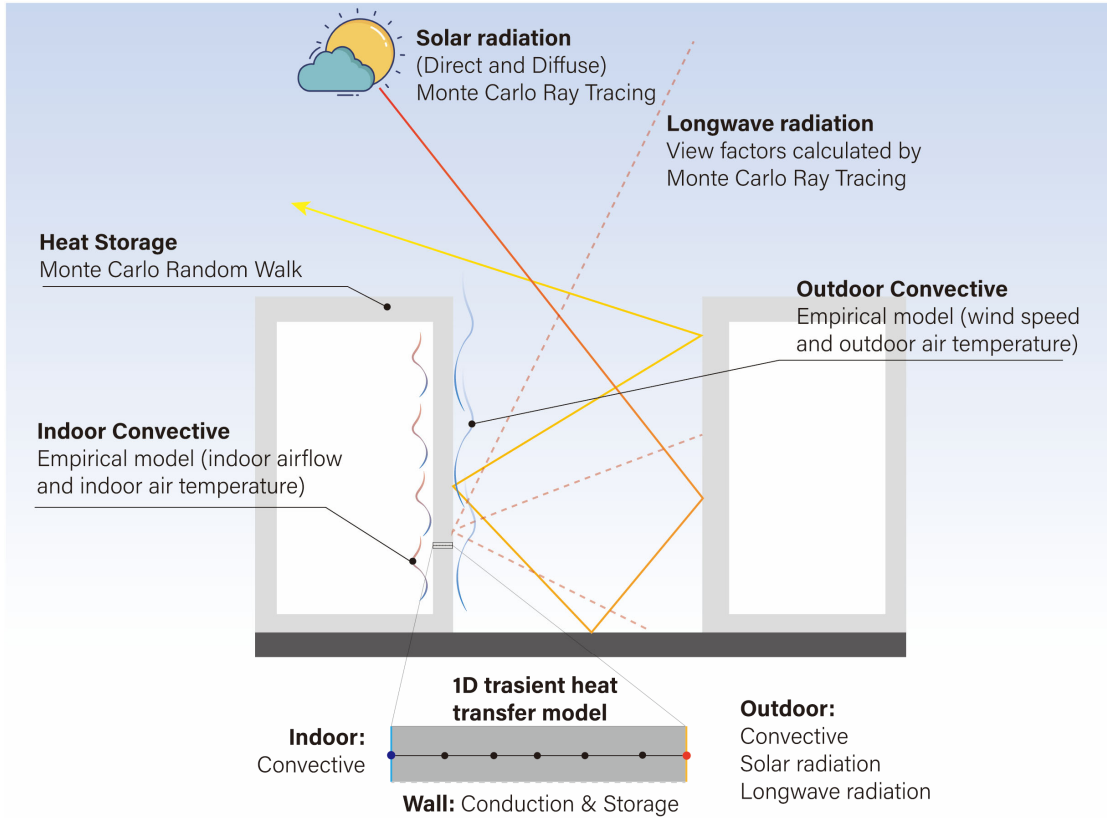
127 **2. Model design**

128 The main objective of GUST is to resolve the coupled radiative–convective–conductive heat transfer
129 processes occurring across complex urban geometries. These coupled processes represent one of the core
130 physical mechanisms driving the urban heat island effects (Manoli et al., 2019). The model is developed
131 based on reduced-scale outdoor measurements conducted within a simplified urban environment (Hang
132 and Chen, 2022). In this experimental setup, complex glazing systems and green infrastructure are
133 intentionally excluded to isolate and validate the core radiative–convective–conductive heat transfer
134 mechanisms. GUST uses a time-dependent heat conduction model to couple radiative, convective, and
135 conductive heat transfer processes. GUST aims to resolve the urban surface temperature by a transient
136 heat conduction model, as illustrated in Fig. 1.

137 The convective and radiative heat transfer at urban surfaces is treated as boundary conditions for the 1D
138 heat conduction model. For the outdoor side, the heat flux (q_{out}) is the sum of radiative (longwave q_l
139 and solar q_s) and convective heat flux ($q_{c,out}$).

140
$$q_{out} = q_l + q_s + q_{c,out} \quad (1)$$

141 The absorbed solar radiation, q_s is the sum of direct solar irradiation ($q_{s,o}$) and diffuse solar irradiation
142 ($q_{s,r}$), expressed by: $q_s = q_{s,o} + q_{s,r}$. The longwave radiation flux q_l includes the radiation between
143 urban surfaces ($q_{l,urban}$) and between urban surfaces and the sky ($q_{l,sky}$), represented as $q_l = q_{l,urban} +$
144 $q_{l,sky}$.



145

146 **Figure 1: The model design of GUST. In this model, 1D transient conductive heat transfer is considered for**
 147 **urban surfaces the system (e.g., walls, roofs, and ground). They are composed of multiple layers where the**
 148 **thermal properties are uniform and isotropic. All urban surfaces are assumed to be opaque in this study.**

149 In this model, all urban surfaces are represented as triangular facets in STL format, with each triangular
 150 facet treated as a single element. Ray tracing and heat-conduction calculations are performed at the
 151 centroid of each element. The spatial resolution of the simulation can be refined by using smaller
 152 triangular facets, thereby increasing the number of elements. Fig. 6 illustrates the triangulated
 153 representation of the urban surfaces.

154 **2.1. Conduction sub-model**

155 The Monte Carlo random walking method is used to solve the 1D heat conduction ([Talebi et al., 2017](#)).
 156 Compared to finite volume method, this approach is insensitiv~~ity~~ to the complexity of urban geometry
 157 and boundary conditions ([Villefranque et al., 2022](#); [Caliot et al., 2024](#)). In the present version, the heat
 158 conduction along the wall span is neglected. The one-dimensional (1D) transient heat conduction
 159 equation is:

160
$$\frac{\partial}{\partial t} T = \alpha \frac{\partial^2 T}{\partial x^2} \quad (2)$$

161 where $\alpha = \frac{k}{\rho c_p}$ is the solid thermal diffusivity and k the thermal conductivity, ρ the density, c_p the
 162 specific heat capacity. The ground, walls and roofs are composed of multiple layers. In the Monte Carlo
 163 random walking method, the heat conduction equation is replaced by finite difference approximation as:

164
$$T(x, t + \Delta t) = P_t T(x, t) + P_{x-} T(x - \Delta x, t + \Delta t) + P_{x+} T(x + \Delta x, t + \Delta t) \quad (3)$$

165 where $P_t = \frac{1}{1+2Fo}$ is defined as probability of time step; $P_{x-} = P_{x+} = \frac{Fo}{1+2Fo}$. where P_{x-} and P_{x+}
 166 respectively represent the probabilities of stepping to the points $(x - \Delta x, t)$ and $(x + \Delta x, t)$. Here,
 167 $Fo = \frac{k\Delta t}{\rho c_p (\Delta x)^2}$ These coefficients are nonnegative probabilistic values and

168
$$P_t + P_{x-} + P_{x+} = 0 \quad (4)$$

169 The Monte Carlo random walking algorithm is schematically illustrated in Fig. 2. The core idea is that
 170 particles walk by following rules:

171 1) Start a random walk at point x .

172 2) Generating a random number (R) between 0 and 1.

173 3) Determine walking direction by conditions

174
$$\begin{cases} 0 < R < P_{x-}: & x \rightarrow (x - \Delta x) \\ P_{x-} < R < (P_{x-} + P_{x+}): & x \rightarrow (x - \Delta x) \\ (P_{x-} + P_{x+}) < R: & x \rightarrow (x), T(i) = T(i) + T(x, t - \Delta t) \end{cases} \quad (5)$$

175 4) If the next point is not on the boundary repeat step 2 and 3 and if it is on the boundary, record $T(i) =$
 176 $T(i) + T$ at the boundary and go to step 1.

177 5) After N random walking, temperature at point x is calculated by

178
$$T(x) = \frac{T(i)}{N} \quad (6)$$

179 When a particle reaches a heat flux, convective or interface boundary, its movement follows the following
 180 rules.

181 1) Heat flux boundary

182 When the particle walks to the boundary of heat flux (q), it is bounced back and record the temperature

183 T_{hf} , which is calculate by $T_{hf} = \frac{q\Delta x}{k} + \frac{q}{2k}(\Delta x)^2$.

184 2) Convective boundary

185 The heat flux of a convective boundary is calculated by $q = h(T_w - T_a)$, where h is the heat transfer
186 coefficient and T_w the wall temperature and T_a the air temperature. The wall temperature is calculated
187 by

188

$$T_w = \frac{1}{1+Bi}T(x - \Delta x) + \frac{Bi}{1+Bi}T_a \quad (7)$$

189 Where $P_x = \frac{1}{1+Bi}$, $P_a = \frac{Bi}{1+Bi}$, $Bi = \frac{h\Delta x}{k}$. When the particle reaches the convective boundary, a new
190 random number R was generated and moves as follows:

191

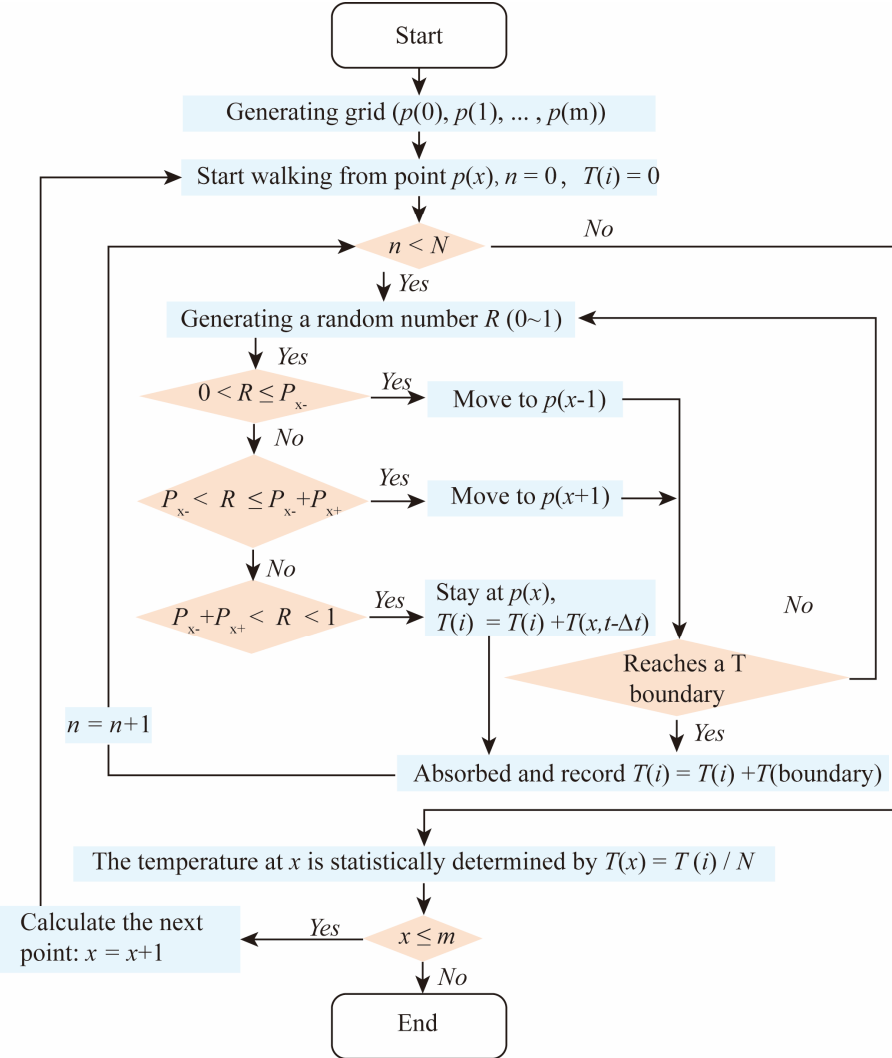
$$\begin{cases} 0 < R < P_x: & \rightarrow \text{bounced back} \\ P_x < R < 1: & \rightarrow \text{absorbed by air with } T(i) = T(i) + T_a \end{cases} \quad (8)$$

192 3) Interface between two layers

193 The interface between layers is flux continuity, i.e. the conductive fluxes are equal on both sides of the
194 interface. The heat conductivities on left and right sides of the interface are k_A and k_B . The conductive
195 heat fluxes on both sides are equal, i.e., $-k_A \frac{dT}{dx} = -k_B \frac{dT}{dx}$. When a particle reaches the interface, it may
196 be reflected or move to the next layer. A new random number R is generated. The particle moves by
197 following

198

$$\begin{cases} 0 < R < P_{x-}: & \rightarrow \text{bounced back to layer A} \\ P_{x-} < R < 1: & \rightarrow \text{move to layer B} \end{cases} \quad (9)$$

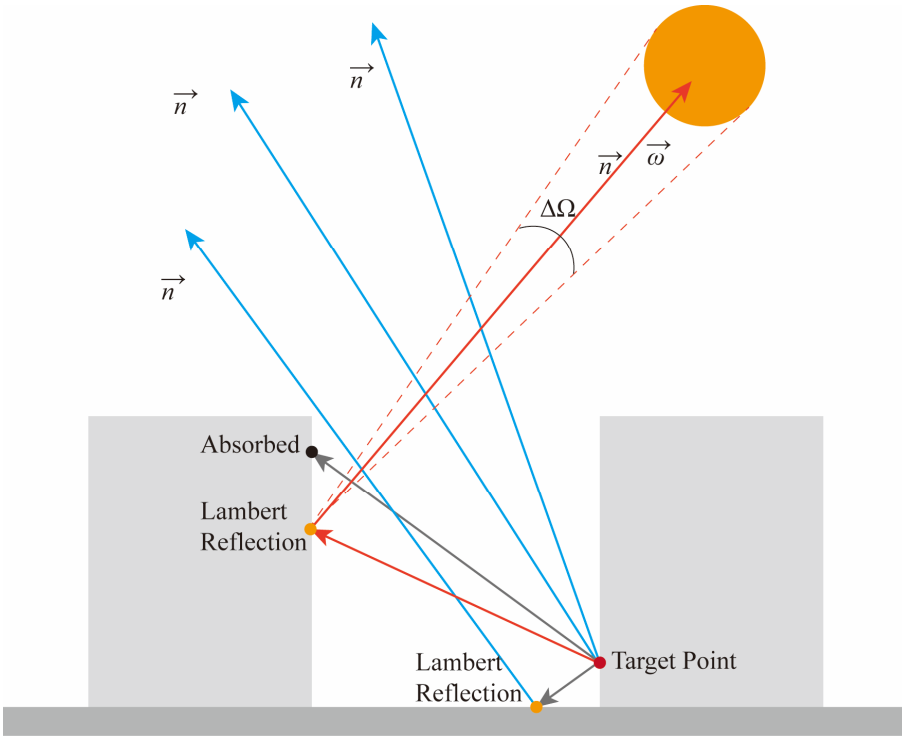


199

200 **Figure 2: Flowchart of the Monte Carlo random walking algorithm for 1D heat conduction. At each point,**
 201 **the particle movement stops after N random walks. Each walk stops when particle either reaches a fixed**
 202 **temperature boundary or remains stationary. Orange diamonds indicate decision points with two possible**
 203 **outcomes (Yes/No).**

204 **2.2. Solar radiation sub-model**

205 The solar radiation q_s is calculated on each triangular facet using the reverse Monte Carlo Ray Tracing
 206 (rMCRT) method, which inherently accounts for both shaded and sunlit areas. In the rMCRT, the ray
 207 starts from the target points, instead of starting from the sky or sun in the ray tracing method ([Caliot et al., 2024](#)). This method ensures that enough photons reach the target point to obtain a statistical result.



209

210 **Figure 3: Schematic illustration of the reverse MCM ray tracing method for calculating the direct and diffuse**
 211 **solar radiation.**

212 The procedure of reverse MCRT is schematically explained in Fig. 3. In total, N photons leave the target
 213 point in random directions (\vec{r}), which is determined by the azimuth θ_a and incidence angle η_a . These
 214 angles are calculated by $\theta_a = 2\pi R_1$ and $\eta_a = \arccos(1 - 2R_2)$, where R_1 and R_2 are random
 215 numbers between 0 and 1.

216 When a photon reaches the surface, it can be absorbed or reflected via Lambert's law. To determine
 217 whether this photon is absorbed, a random number R_{ab} (ranging from 0 ~ 1) is generated. When $R_{ab} >$
 218 α_s (surface albedo), the photon is absorbed by the surface. When $R_{ab} < \alpha_s$, the photon is reflected. All
 219 surfaces are considered Lambertian and the direction of reflect solar beam is determined by the azimuth
 220 θ_a and incidence angle η_a of that surface. At each reflection, θ_a and η_a are recalculated by
 221 regenerating new random numbers.

222 When the photon reaches the “sky” in the direction of \vec{r} , its angle (θ_{ns}) with the reverse solar direction
 223 $\vec{\omega}_{sun}$ is calculated. When $\theta_{ns} < \Delta\Omega_a$, that photon is marked as reaching the “Sun”, otherwise, that
 224 photon is marked as reaching the “Sky”. The direct ($q_{s,o}$) and diffuse ($q_{s,r}$) solar radiation reaching the

225 target point can then be statistically determined by:

$$226 \quad q_{s,o} = \frac{\pi I_{s,o}}{\Delta\Omega_d N} \sum_{\theta_{ns} < \Delta\Omega_d} \left| \vec{\omega}_{sun} \cdot \vec{n} \right| \quad (10)$$

$$227 \quad q_{s,r} = \sum_{\theta_n > d\Delta\Omega_d} \frac{I_{s,r}}{N} \quad (11)$$

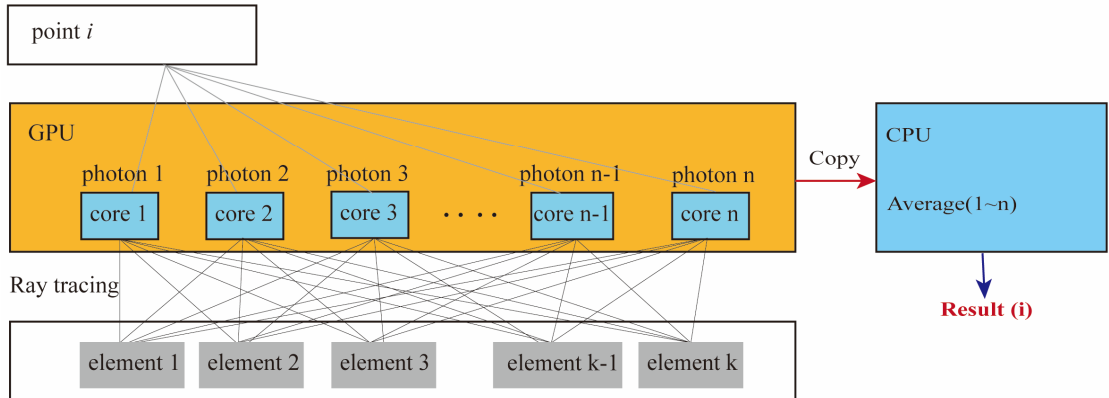
228 where $I_{s,o}$ and $I_{s,r}$ is the direct normal irradiance and diffuse solar radiation. The ratio between the
229 direct and diffuse solar radiation is calculated by the model proposed by ([Reindl et al., 1990](#)).

230 The rMCRT requires a large number of rays to achieve statistically reliable results. To accelerate the
231 simulation, the model is run in parallel on GPUs (Graphics Processing Units) using the CUDA® platform
232 ([Yoshida et al., 2024](#)). The advantage of GPUs is that they have a large number of cores, which enables
233 them to handle many parallel tasks simultaneously. GPUs are particularly well-suited for accelerating
234 MCRT, since each ray tracing operation is independent.

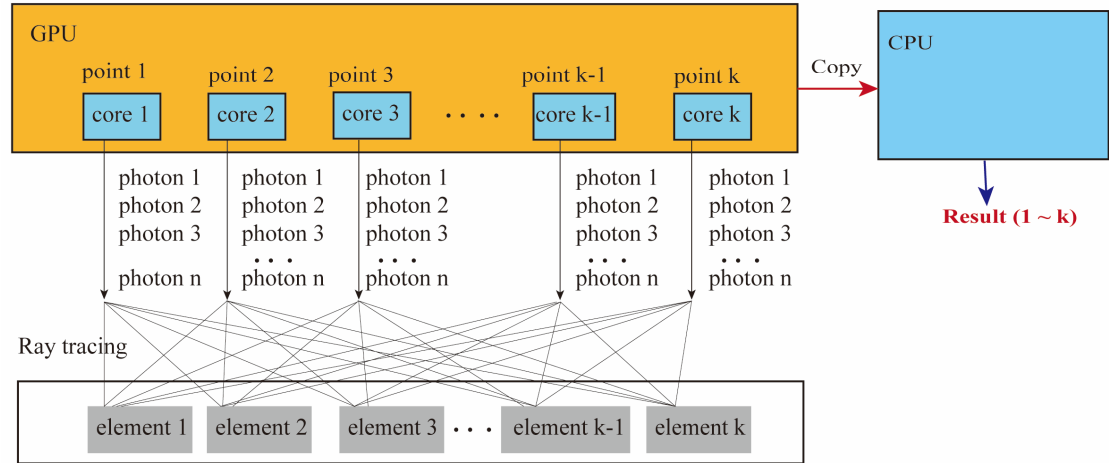
235 The GPU parallel computing is executed using two strategies, depending on the total number of elements.
236 As illustrated in Fig. 4, Strategy 1 calculates the radiative flux point by point, emitting n photons for
237 ray tracing simulation. Each photon is processed in a separate GPU core. Once the ray tracing process is
238 complete, the results from the GPU cores are copied to the CPU, where radiative flux at each point is
239 calculated. Strategy 2 calculates the radiative flux for all points simultaneously, with each GPU core
240 computing the flux for a single point. The ray tracing of n photons is performed iteratively on the GPU.

241 The advantage of Strategy 1 is the efficient utilization of GPU cores when the number of points and
242 elements is small. However, its disadvantage is that it requires a large amount of memory when the
243 number of points is large. In contrast, Strategy 2 requires significantly less memory and only transfers
244 data to the CPU once, making it highly efficient when the number of points and elements is large.

(a) Strategy 1



(b) Strategy 2



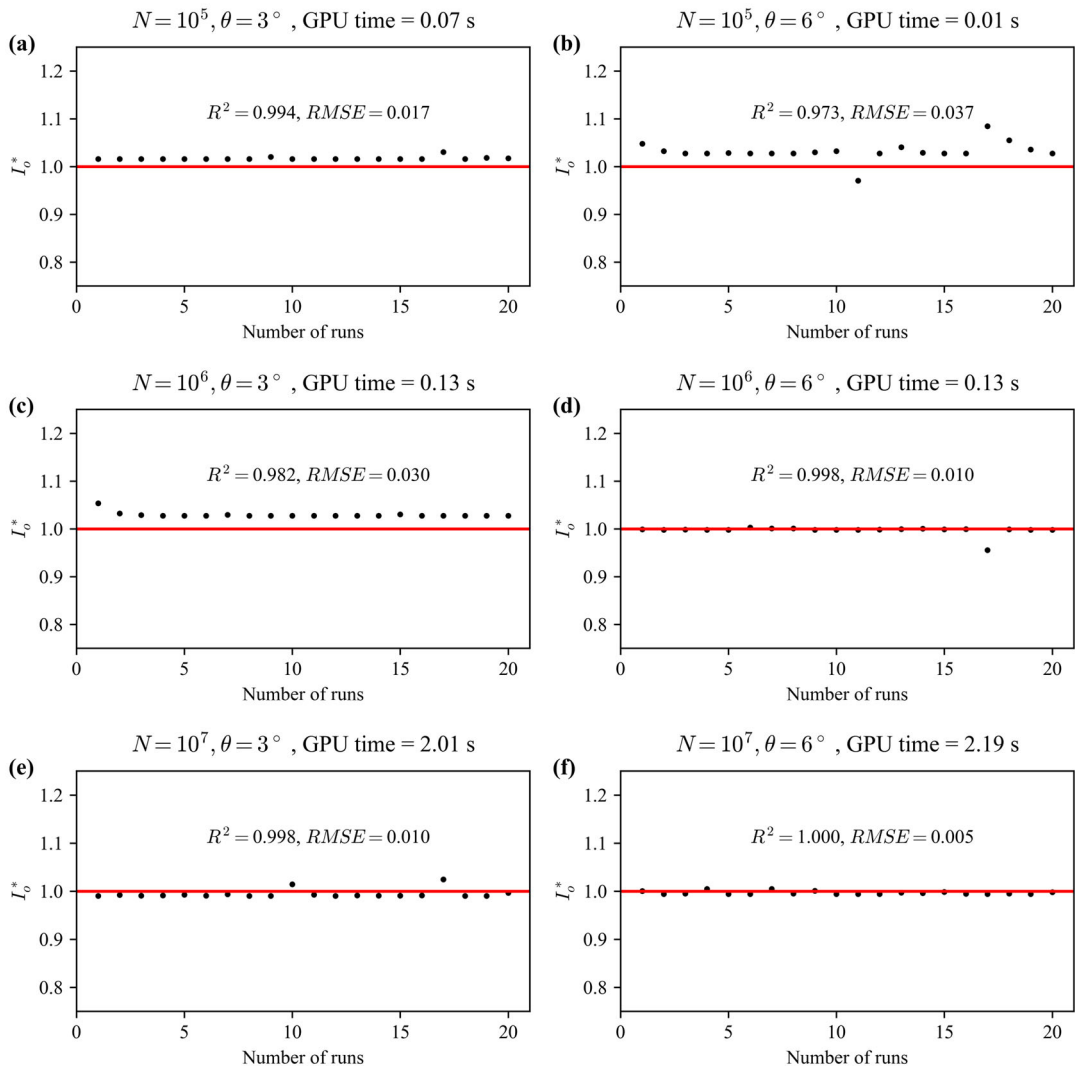
245

246 **Figure 4: Two strategies for GPU parallel computing. (a) The ray tracing is conducted point by point. For**
 247 **each point, n photons are emitted. Each GPU core calculates one photon. (b) The ray tracing is conducted**
 248 **for all points at one time. Each GPU core calculates one point. The ray tracing of n photons is performed**
 249 **iteratively within the GPU core.**

250 The space angle of the Sun ($\Delta\Omega_d$) and the number of photons (N) can significantly affect the accuracy of
 251 reverse MCM. To evaluate this influence, a series of test cases are conducted, in which the direct solar
 252 radiation at a ground point is calculated. The solar radiation on the open ground can be calculated
 253 theoretically, as there is no shading from buildings.

254 Figure 5 shows the errors of simulations using different values of N and $\Delta\Omega_d$. The simulation time of
 255 each case is also indicated in that figure. When the number of photons is increased from $N = 10^5$ to
 256 $N = 10^7$, the simulation time increases from 0.05s to 1.15s, which is an increase of 23 times. The

257 relatively slow increase in simulation time is a result of the parallel computing capabilities of the GPU.
 258 In each scenario, the model was run 20 times to observe the difference between each run.
 259 A small $\Delta\Omega_d$ reduce the photon number reaching the Sun, thus increasing the error, where the $\Delta\Omega_d$ is
 260 calculated from a 2D angle θ as $\Delta\Omega_d = 2\pi(1 - \cos(\theta))$. For example, the error in cases with $\theta = 3^\circ$
 261 greater than that in cases with $\theta = 6^\circ$. A larger number of photons is needed to compensate for this error.
 262 For example, the case with $\theta = 3^\circ$ and $N = 10^7$ shows acceptable accuracy. However, the case with
 263 $\theta = 6^\circ$ shows a comparable accuracy when $N = 10^6$ and takes less simulation time.
 264 In the subsequent simulations, $\theta = 6^\circ$ and $N = 10^6$ are applied to balance accuracy and simulation
 265 time.



266

267 **Figure 5: Numerical errors of direct solar radiation estimation using Monte Carlo method. The simulated**
 268 **solar radiation ($I_{o, sim}$) is normalized by the true value ($I_{o, true}$) and is expressed by ($I_o^* = \frac{I_{o, sim}}{I_{o, true}}$), where $I_o^* =$**
 269 **1.0 represents an exact reproduction of the solar radiation. The test cases use different space angles of sun**
 270 **$\Delta\Omega_d = 2\pi(1 - \cos(\theta))$ and photon numbers (N). The red lines represent the true value, and dots represent**
 271 **the simulated data.**

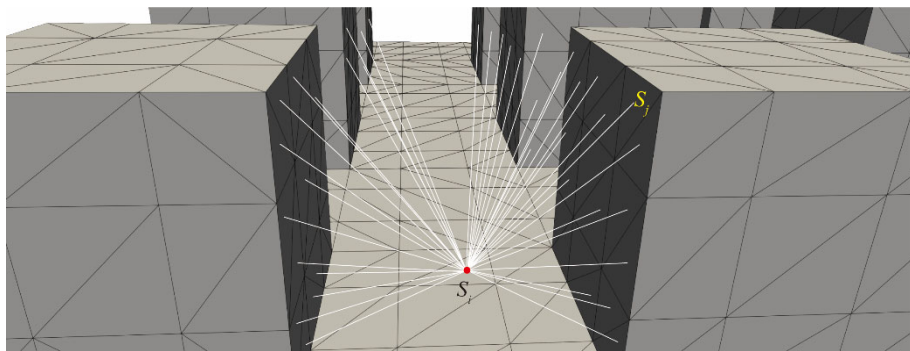
272 **2.3. Longwave radiation sub-model**

273 The view factors between the surfaces, as well as from the surfaces to the sky, are also calculated using
 274 the Monte Carlo ray tracing model, as illustrated in Fig. 6. The urban surfaces are divided into multiple
 275 triangular elements N_{ur} . The view factor from element S_i to element S_j , denoted as $F_{i,j}$, is calculated
 276 by emitting N photons from the centroid of element S_i . The algorithm then counts the number of
 277 photons $n_{i,j}$ that reach element S_j . Finally, the view factor $F_{i,j}$ is calculated by $F_{i,j} = n_{i,j}/N$. The sky
 278 view factor is also determined in this approach by treating the sky as an urban surface.

279 The longwave radiative heat exchange between the surfaces, as well as from the surfaces to the sky, is
 280 calculated by:

$$281 \quad q_l = F_{i,sky}\varepsilon(R_{l,in} - \sigma T_i^4) + \varepsilon\sigma \sum_{j=1}^{j=N_{ur}} F_{i,j}(T_j^4 - T_i^4) \quad (12)$$

282 where ε is the material emissivity, σ is Stefan–Boltzmann constant ($= 5.67 \times 10^{-8}$) ($\text{W m}^{-2} \text{ K}^{-4}$), $R_{l,in}$ is
 283 the downward longwave radiation from the sky, $F_{i,sky}$ is the sky view factor of element S_i . The surface
 284 temperature from the previous step (T_i and T_j) is used to calculate the longwave radiative heat exchange.



286 **Figure 6: Schematic illustration of how view factors are calculated between urban surface elements.**

287 **2.4. Outdoor convective sub-model**

288 GUST does not calculate urban airflow; instead, it uses empirical formulas to calculate the outdoor
 289 convective heat flux as follows:

290
$$q_{c,out} = U_f h_{out} (T_{w,out} - T_{a,out}) \quad (13)$$

291 where $T_{a,out}$ is the outdoor air temperature in the canopy layer, U_f is the wind speed, and convective
 292 heat transfer coefficient $h_{out} = 4.5 \left(\frac{ws}{m^3 K} \right)$ is adopted.

293 The wind speed above the urban canopy layer (UCL) is calculated by a logarithm wind profile:

294
$$U(z) = \frac{u_*}{\kappa} \ln \left(\frac{z + z_0}{z_0} \right) \quad (14)$$

295 where $z_0 = 0.1H$ based on the estimation of ([Grimmond and Oke, 1999](#)).

296 The wind speed within the UCL is assumed to be uniform and is calculated by the model by Bentham
 297 and Britter ([Bentham and Britter, 2003](#)). This model estimates the in-canopy velocity (U_c) based on the
 298 frontal area density (λ_f) as follows:

299
$$\frac{U_c}{u_*} = \left(\frac{2}{\lambda_f} \right)^{0.5} \quad (16)$$

300 Here, the friction velocity (u_*) depends on the urban morphology and is estimated using the following
 301 functions ([Yuan et al., 2019](#)):

302
$$\begin{cases} u_* = 0.12U_{2H}, & \text{for } (\lambda_f > 0.4) \\ u_* = 6.7U_{2H}^3 - 6.4U_{2H}^2 + 1.7U_{2H} + 0.03, & \text{for } (\lambda_f < 0.4) \end{cases} \quad (17)$$

303 where U_{2H} is the wind speed at a height of $2H$ above the ground, and H is the building height.

304 The air temperature in UCL is assumed to be uniform and calculated by the urban canopy model ([Yuan
 305 et al., 2020](#)). This model estimates the in-canopy temperature based on the exchange velocity U_E and
 306 sensible heat flux $q_{c,out}$.

307
$$T_c = \frac{1}{D_c} \frac{q_{c,out}}{U_{2H}(1 - \lambda_p)} \left(1 - 0.12 \left(\frac{2}{\lambda_f} \right)^{0.5} \right) + T_{a,2H} \quad (18)$$

308 where $D_c = 17.183$, is a heat capacity constant of the air, $T_{a,2H}$ is the air temperature above the roof
 309 level, λ_p is the plan area density. Bentham and Britter ([Bentham and Britter, 2003](#)) suggested that the
 310 U_E can be calculated by:

$$311 \quad \frac{U_E}{u_*} = \left(\frac{U_{2H} - U_c}{u_*} \right)^{-1} \quad (19)$$

312 The $q_{c,out}$ is calculated by the temperature from previous time step.

313 2.5. Indoor sub-model

314 The indoor side uses a convective boundary condition given by $q_{in} = h_{in}(T_{w,in} - T_{a,in})$, where $T_{a,in}$ is
 315 the indoor air temperature, $T_{w,in}$ is the wall temperature on indoor side. The indoor heat transfer
 316 coefficient $h_{in} = 13.5 \frac{W}{m^2 K}$ accounts for both natural convection and longwave radiative heat flux.

317 For air-conditioned rooms, the indoor air temperature is assumed to be constant at $T_{a,in} = 26$ °C. In
 318 contrast, for naturally ventilated rooms, the indoor air temperature is assumed to be equal to the in-canopy
 319 air temperature, represented as $T_{a,in} = T_c$.

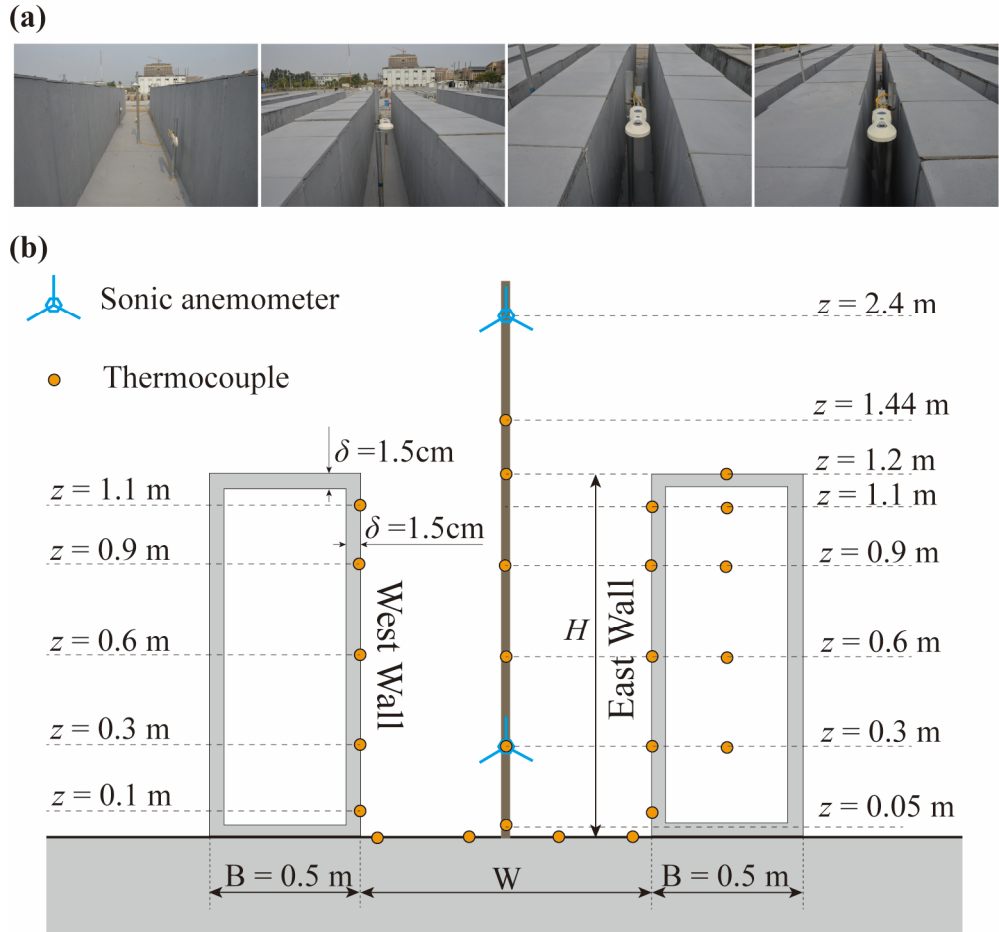
320 3. Model validation and assessment

321 3.1. SOMUCH measurement

322 The model is validated by cross-compare with the SOMUCH measurement, which is a scale outdoor
 323 field measurement conducted in Guangzhou, P.R. China (23°1' N, 113°25' E) ([Hang and Chen, 2022](#);
 324 [Hang et al., 2025](#); [Wu et al., 2024](#)). This measurement provides a quality database for evaluating urban
 325 climate models ([Hang et al., 2024](#); [Chen et al., 2025](#)). The campaign conducted from 29th Jan to 1st
 326 Feb 2021 is used. In that campaign, both surface and air temperatures were measured at high resolution,
 327 making it an ideal database for validating current models.

328 The geometry of the building blocks and measurement points are plotted in Fig. 7. In that measurement,
 329 the urban buildings are modeled by hollow concrete blocks with a size of 0.5 m × 0.5 m × 1.2 m and a
 330 thick of 0.015 m. The blocks are arranged to form street canyons with four different aspect ratios, i.e.,
 331 H/W = 1, 2, 3, 6. Each row consists of 24 blocks and has a length of L = 12 m. In the experiment, the
 332 surface and air temperatures are measured using thermocouples (Omega, TT-K-36-SLE, Φ0.127 mm and

333 TT-K- 30-SLE, $\Phi 0.255$ mm). The wind speeds inside and above the street canyon are measured using
 334 sonic anemometers (Gill WindMaster). The incoming longwave and solar radiation are measured using
 335 weather stations (RainWise PortLog). The thermal characteristics of the concrete and ground are listed
 336 in Table 1.



337

338 **Figure 7: Photograph of the SOMUCH experiment (a). The geometry of concrete blocks and measurement**
 339 **points in SOMUCH (b). The thermocouples are used to measure the surface temperature and air temperature.**
 340 **The sonic anemometers are used to measure wind speed.**

341

342 **Table 2. Thermal properties of the building material. The emissivity is for the longwave radiation and albedo**
 343 **is for the solar radiation.**

| Material | Density ρ (kg m ⁻³) | Conductivity k (W m ⁻¹ K ⁻¹) | Specific Heat Capacity c_p (J kg ⁻¹ K ⁻¹) | Emissivity ϵ | Albedo α |
|----------|---|--|---|--------------------------|--------------------|
| Concrete | 2420 | 2.073 | 618 | 0.87 | 0.24 |

344

345 **3.2. Cross comparison of the roof temperature**

346 The surface temperature model is validated by cross-comparing with SOMUCH measurement. Many
 347 factors affect the accuracy of the model, including the radiation, convective and conduction. To
 348 separately investigate these factors, the temperatures at roofs are first validated because the total radiative
 349 flux of roof is only influenced by the incoming longwave and solar radiation. The shading effect of other
 350 blocks can be ignored as the block heights are uniform. Therefore, the accuracy of conductive and
 351 convective sub-models can be separately evaluated.

352 The accuracy of this model is quantitatively evaluated by two statistical parameters, the root mean square
 353 error (RMSE), and coefficient of determination (R^2). The RMSE and R^2 of u_x^* are calculated by:

$$354 \quad \text{RMSE} = \sqrt{\frac{1}{n} \sum_{i=1}^n (O_i - P_i)^2} \quad (21)$$

$$355 \quad R^2 = 1 - \frac{\sum_{i=1}^n (O_i - P_i)^2}{\sum_{i=1}^n (O_i - \bar{O}_i)^2} \quad (22)$$

356 where O_i represents the measured values, P_i is the simulated values, \bar{O}_i is the mean of the measured
 357 values, and n is the number of data points.

358 The wind speed at roof level is needed to calculate the outdoor convective flux of roofs. In SOMUCH
 359 measurement, the wind speed was measured above the roof and at a height of $2H$. The wind speed at
 360 roof level is estimated by a logarithm wind profile as:

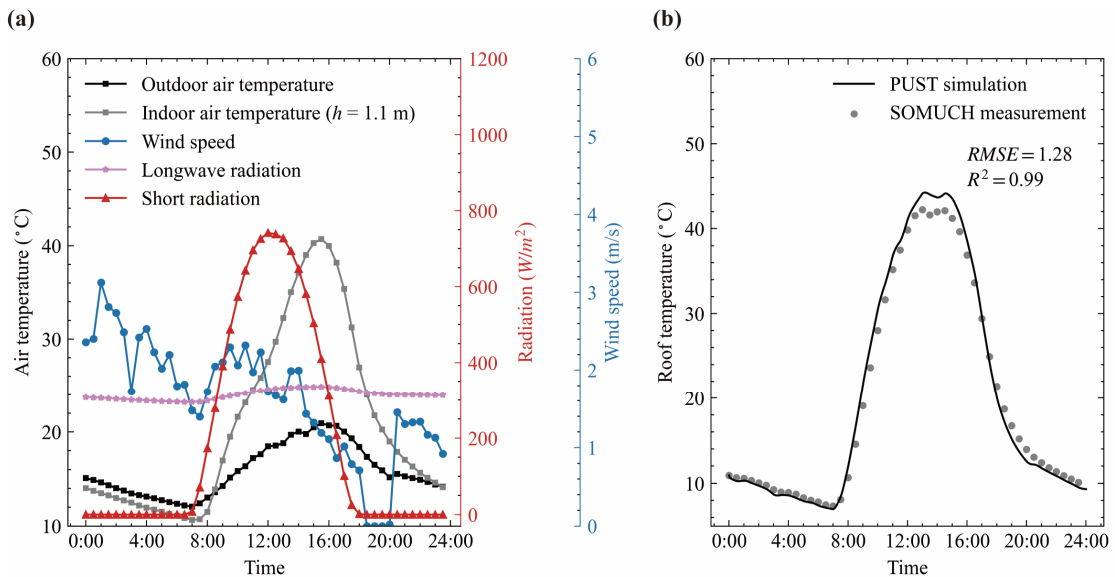
361

$$U(z) = \frac{u_*}{\kappa} \ln \left(\frac{z + z_0}{z_0} \right) \quad (23)$$

362 where $z_0 = 0.1H$ based on the estimation of (Grimmond and Oke, 1999). The wind velocity at roof
 363 level ($z = H$) can be calculated by $\frac{U_H}{U_{2H}} = 0.787$. The outdoor air temperature, incoming solar and
 364 longwave radiation, are from the weather station ($z = 2H$).

365 For the indoor side, the radiative flux between indoor surfaces is ignored in this model. Only the
 366 convective flux is modeled. The convective velocity is assumed to be 3 m/s and CHTC is assumed to be
 367 4.5 for indoor side. Data from the indoor measurement point at $H = 1.1$ m is used. That point is the
 368 nearest measurement point to the roof.

369 Figure 8(a) plotted shows the measurement data that was used to drive the model. During the
 370 measurements, the building model was enclosed, leading to the development of very high indoor
 371 temperatures. Therefore, the measured indoor air temperature was used as an input for the validation
 372 simulation. Fig. 8(b) shows the roof surface temperatures from measurement and simulation. Generally,
 373 the roof surface temperatures are well reproduced by the model, because the R^2 is 0.99 and $RMSE$ is
 374 1.28. The large discrepancy is found around noon. The model slightly overestimates the roof temperature.
 375 The comparison of roof temperatures shows that the conductive and convective sub-models are reliable.



376

377 **Figure 8: Weather data on the measurement date (29 January 2021) is shown in (a). Panel (b) compares roof**
 378 **surface temperatures from simulation and measurement, where points denote measured data and lines denote**

379 simulated data.

380 **3.3. Cross comparison of the wall temperature**

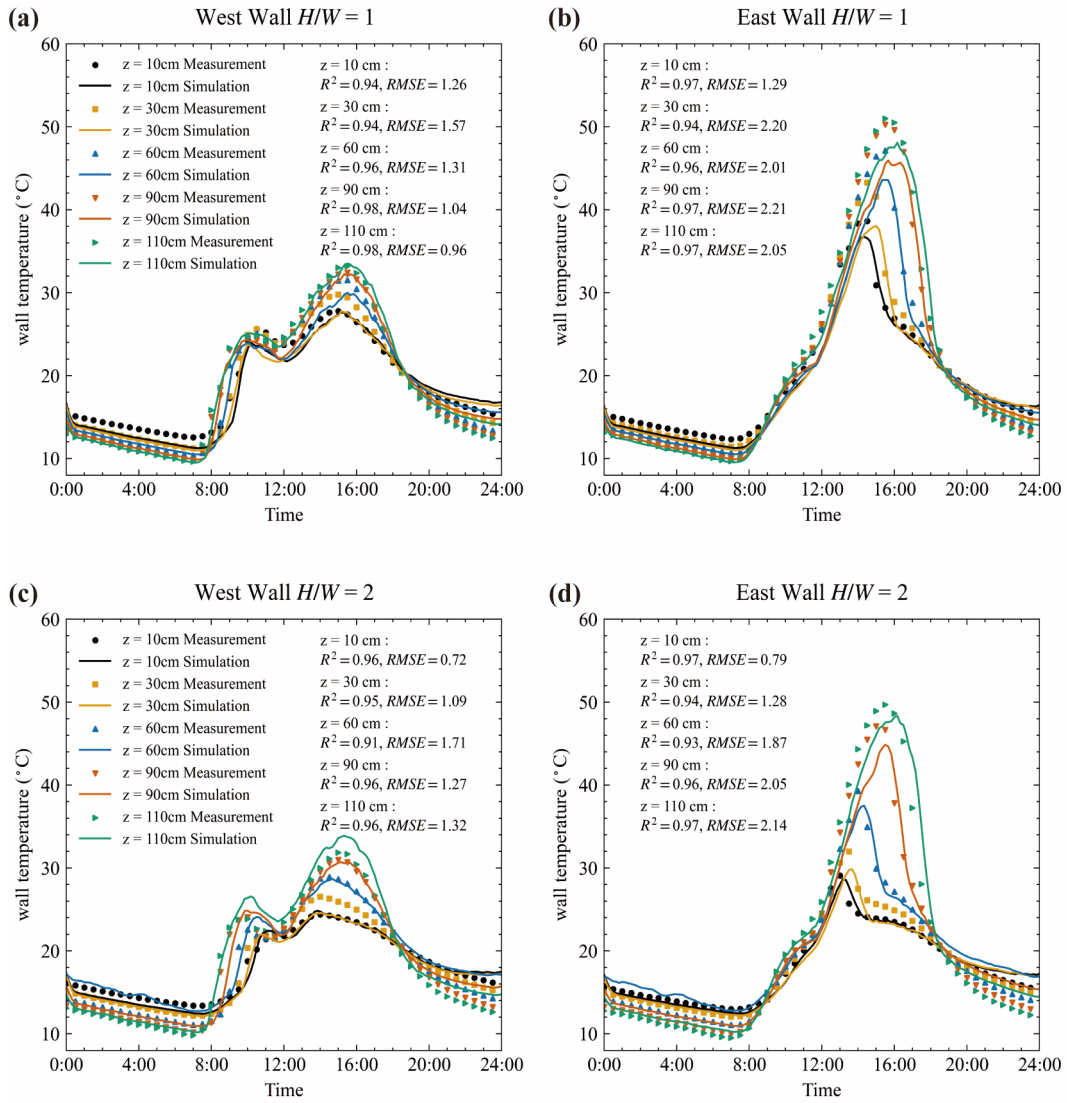
381 The temperatures at walls are more complicated than those at the roof because the buildings change the
382 radiative fluxes and wind speeds in street canyons. The radiative fluxes need to be accurately modelled
383 as they are the main energy input and have a large impact on the surface temperature. To avoid the
384 influence of air temperature and wind speed modeling, the canyon air temperature, wind speed, and
385 indoor temperature are from the measurement. The air temperatures are measured from multiple heights.
386 For the convective flux modelling, the nearest measured air temperatures are used. The wind speeds from
387 the sonic anemometer in the street canyon ($z = 0.3$ m) are used to calculate the convective flux at outdoor
388 side. The driving data are plotted in Appendix A.

389 The east and west walls are defined by taking street canyon center as the origin point. The street direction
390 is tilted from north toward east by 25° . Therefore, the west and east walls are roughly defined to
391 distinguish them. The street orientation has been modeled in our model and will not cause additional
392 discrepancy.

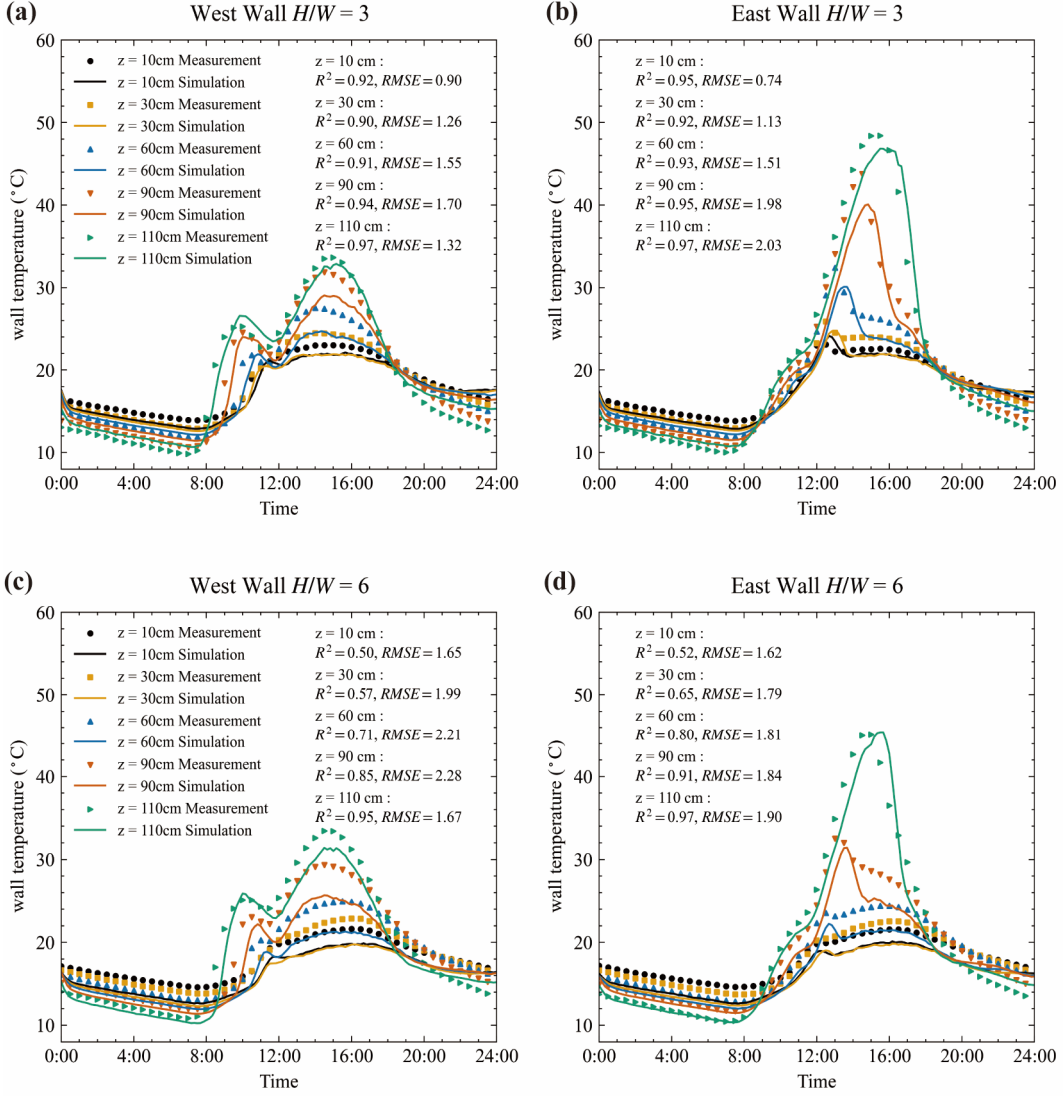
393 Figures 9 and 10 show the comparison of wall temperatures from simulation and measurement. For each
394 surface, multiple points are compared to avoid the influence of localized anomalies and to ensure that
395 the evaluation reflects the overall wall-temperature behavior. Generally, the wall temperatures are well
396 reproduced, particularly their variation trend. The peak hours are well reproduced. For example, there
397 are two temperature peaks for the west wall. The first one is around 10:00 and the second is around 16:00.
398 Both simulation and measurement show the same occurring time.

399 To quantify model performance, the coefficient of determination (R^2) and root-mean-square error
400 (RMSE) were calculated and marked in each sub-figure. Except for the $H/W = 6$ case, the R^2 values
401 exceeded 0.9 for all walls, confirming a strong correlation between simulation and measurement. For
402 $H/W = 6$, R^2 is lower because of nighttime underestimation, although the RMSE remains within the
403 same range as the other cases (1.6 °C to 2.2 °C). The main reason for this discrepancy is that wall
404 temperatures in deep street canyons ($H/W = 6$) show only a slight increase compared to the air
405 temperature, due to minimal sunlight penetration into the canyon. Under these conditions, wall

406 temperatures become particularly sensitive to convective and longwave radiative fluxes, which amplifies
 407 the impact of small modeling uncertainties.



408
 409 **Figure 9: Wall temperature comparison between simulation and measurements for street canyons with aspect**
 410 **ratios of $H/W = 1.0$ and 2.0 . Surface temperatures were measured on 29 January 2021. The root mean square**
 411 **error (RMSE) and coefficient of determination (R^2) are calculated and shown. Symbols denote measurements,**
 412 **while lines indicate simulations. The left panel corresponds to west side walls and the right panel to east side**
 413 **walls.**



414

415 **Figure 10: Wall temperature comparison between simulations and measurements, as in Figure 9, but for street**
 416 **canyons with aspect ratios of $H/W = 3$ and 6.**

417 **3.4. Cross comparison of the ground temperature**

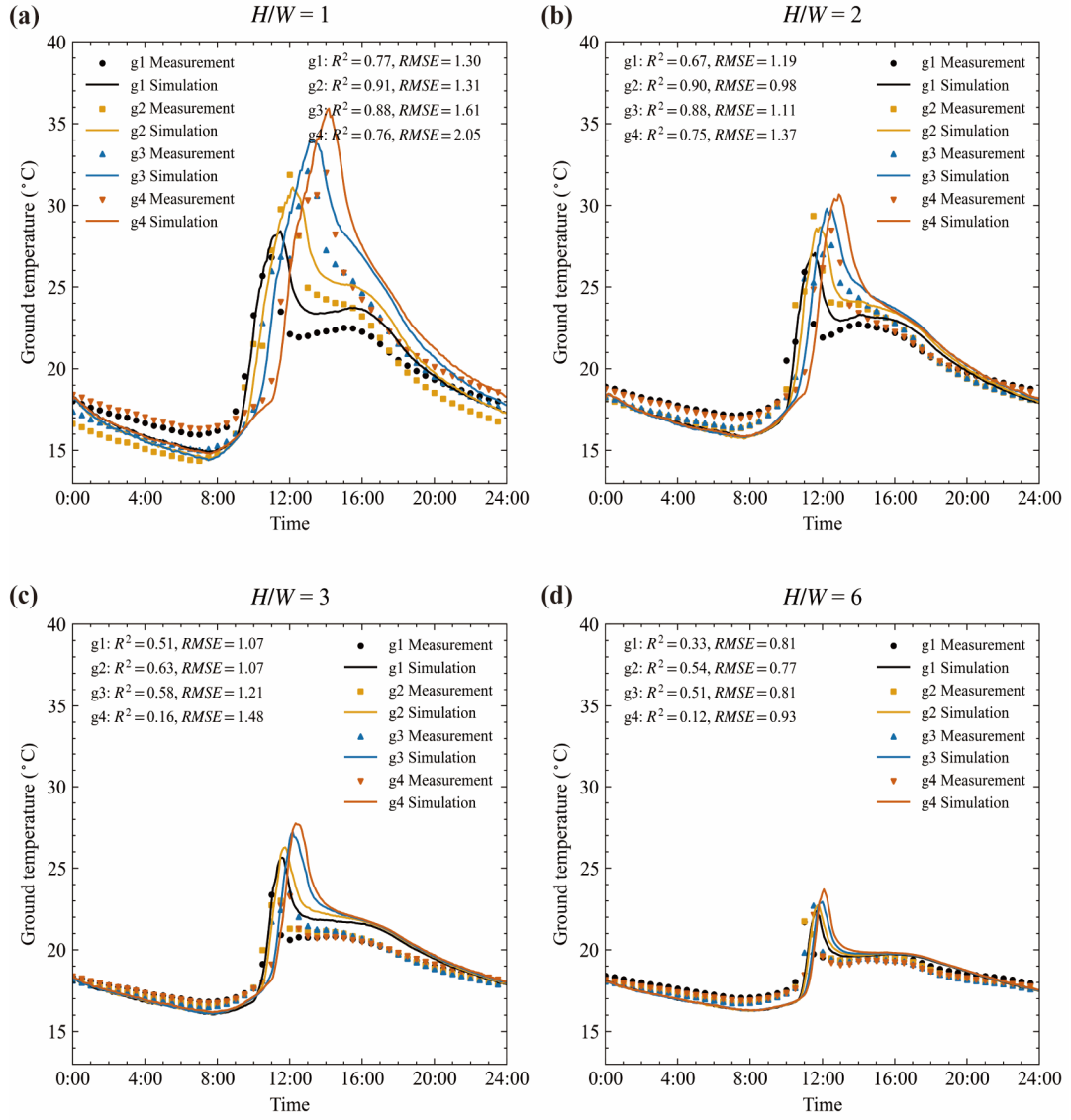
418 The surface temperatures of the ground are heavily influenced by heat storage. During the day, heat is
 419 conducted to deeper layers and stored there. At night, this stored heat is released. Therefore, the initial
 420 temperature field and boundary conditions are critical for accurately modeling surface temperatures. In
 421 this study, an adiabatic boundary condition is applied at a depth of 0.5 m below the ground surface. The
 422 soil material is divided into three layers with thicknesses of 0.2 m, 0.15 m, and 0.15 m. All three layers
 423 are assumed to be made of concrete. The thermal properties in Table 1 are used. The underground

424 temperatures are measured by thermocouples with three depths of 5 cm, 10 cm, and 20 cm, as plotted in
425 Appendix A. In this study, we used only the measured underground temperatures at 0:00 to initialize the
426 underground temperature field. It is important to note that the available soil temperatures were measured
427 in open ground rather than under street canyons. This difference may lead to discrepancies in modeling
428 ground surface temperatures.

429 Figure 11 shows the ground surface temperatures from measurement and simulation. The ground surface
430 temperatures are measured at four locations: g1, which is close to west wall; g4, which is close to east
431 wall; and g2 and g3, which are situated in the middle of the streets. Generally, the temperature variations
432 are well reproduced by the model. For example, peak temperatures occur sequentially from g1 to g4 due
433 to the movement of the building's shadow. This phenomenon is observed in both simulations and
434 measurements.

435 The accuracy of ground temperatures is lower than that of the wall temperatures in terms of R^2 . For
436 example, in $H/W = 2$, the R^2 values for temperatures at the west wall range from 0.91 to 0.97, while
437 those at the ground range from 0.67 to 0.90. However, the ground temperatures can be considered well
438 modeled because the RMSE for ground temperatures is smaller than that for wall temperatures. Using
439 $H/W = 2$ as an example, the RMSE values for the west wall range from 0.69 to 1.71 °C, while those for
440 the ground range from 0.98 to 1.37 °C. This difference between the R^2 and RMSE values is due to the
441 ground temperature increase being much lower than that of the walls because of shading, particularly in
442 deep street canyons.

443 Uncertainties in the input data may also contribute to the discrepancies between simulation and
444 measurement. First, the thermal properties of soil can differ significantly from those of concrete blocks.
445 Secondly, the initial temperature is measured in surrounding area, rather than in street canyons. Thirdly,
446 since the same initial temperature field is used for all four points, the model is unable to reproduce the
447 differences between points at night.



448

449 **Figure 11: Ground temperature comparison between the simulation and measurement results at street canyon**
450 aspect ratio of $H/W = 1.0, 2.0, 3.0$, and 6.0 . Surface temperatures are measured on 29th Jan 2021. The root
451 mean square error (RMSE), and coefficient of determination (R^2) are calculated and plotted. The points
452 represent measured data and lines represent the simulated data.

453

454 **3.5. Surface energy balance analysis**

455 The surface temperature comparison indicates that model uncertainties arise from various factors. To
456 identify the main factors impacting the model accuracy, the energy balance of wall surface is analyzed.

457 The heat fluxes of solar (Q_K), longwave radiation (Q_L), convection (Q_H), and conduction (Q_G) of outer
458 surface of walls satisfy the following equation:

459
$$Q_K + Q_L + Q_G + Q_H = 0 \quad (24)$$

460 Here, the longwave heat flux Q_L is divided into two parts as the heat exchange between wall to sky
461 ($Q_{L,sky}$) and to other urban surfaces ($Q_{L,urban}$), expressed as $Q_L = Q_{L,sky} + Q_{L,urban}$. This analysis aims
462 to determine whether it is necessary to model the longwave heat exchange between urban surfaces, which
463 requires substantial computational resources.

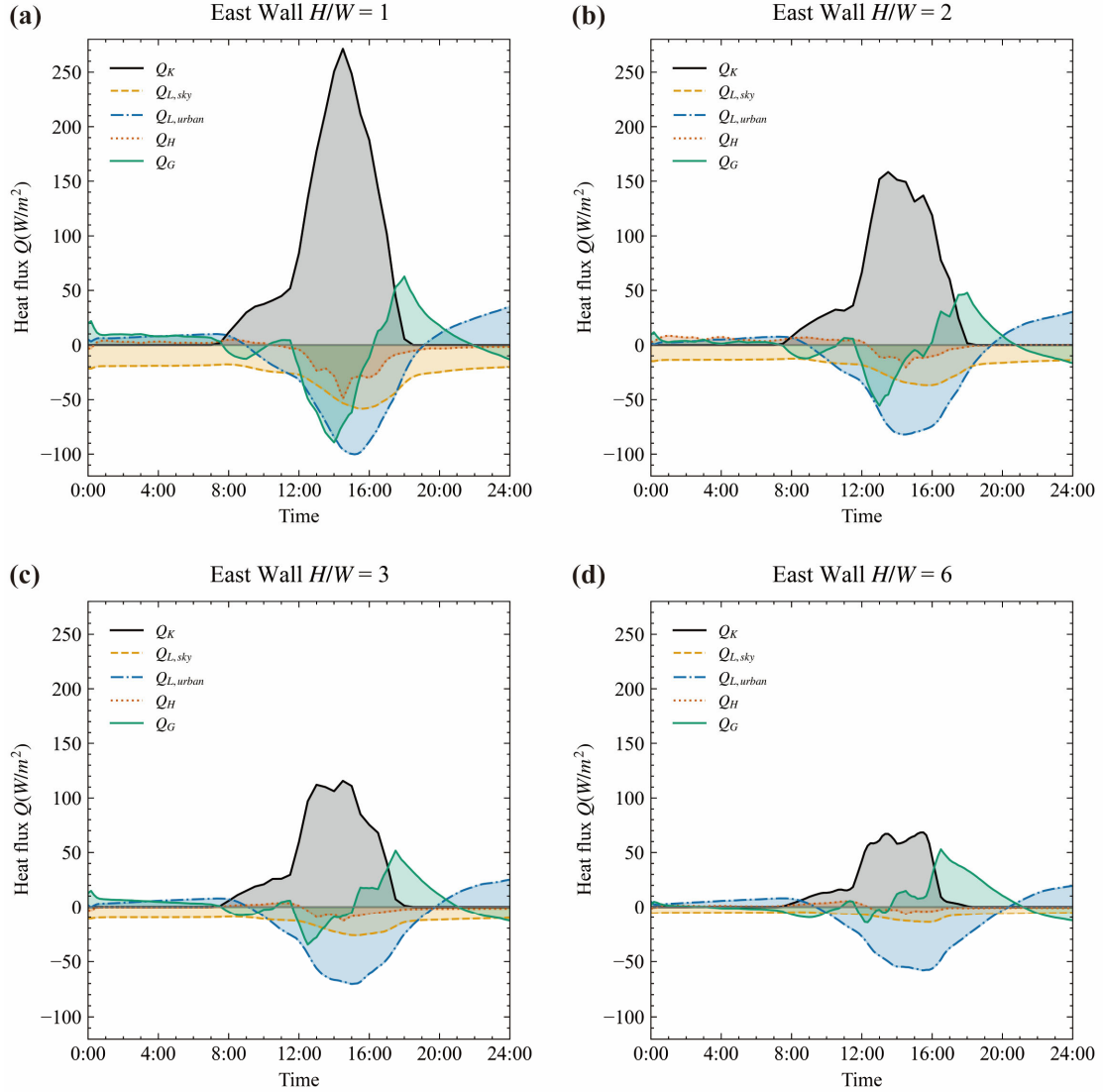
464 Figures 12 and 13 show the heat fluxes of walls in the simulation. The heat fluxes of east and west walls
465 are averaged from five measurement points on each. Our previous work ([Mei et al., 2025](#)) ~~demonstrated~~
466 ~~that the MCRT can accurately predict solar radiation in high-density urban configurations, while also~~
467 ~~achieving high computational efficiency through GPU-based acceleration. demonstrated that a Monte~~
468 ~~Carlo ray tracing approach accurately predicts incident solar radiation.~~ In that study, we compared the
469 albedo of the urban canopy layer and of street canyons across a range of urban layouts with in-situ
470 measurements, achieving excellent agreement. ~~The previous study also serves as an independent~~
471 ~~validation of the ray-tracing component within the modeling framework. Although the ray-tracing~~
472 ~~procedure in the present study differs from that in our previous work, the core computational framework~~
473 ~~remains the same. In the previous study, solar rays were emitted directly from the sun and sky, whereas~~
474 ~~in this study, we adopted a reverse ray-tracing technique, in which rays are emitted from building surfaces~~
475 ~~toward the surrounding environment.~~

476 In all cases, longwave radiative heat exchange between urban surfaces plays an important role in the
477 energy balance, particularly at high aspect ratios. The longwave radiative fluxes from sky only contribute
478 a small amount of total longwave radiative flux in $H/W = 6$, as shown in Fig. 12(d) and Fig. 13(d). The
479 shading effect of buildings creates heterogeneous surface temperatures within the urban canopy layer.
480 The large temperature differences between surface elements contribute a large portion of the total heat
481 flux. This highlights the necessity for accurate modeling of longwave heat exchange between urban
482 surfaces, even though it demands significant computational resources.

483 The conductive heat flux also contributes a large portion of the total heat flux. It is negative in the

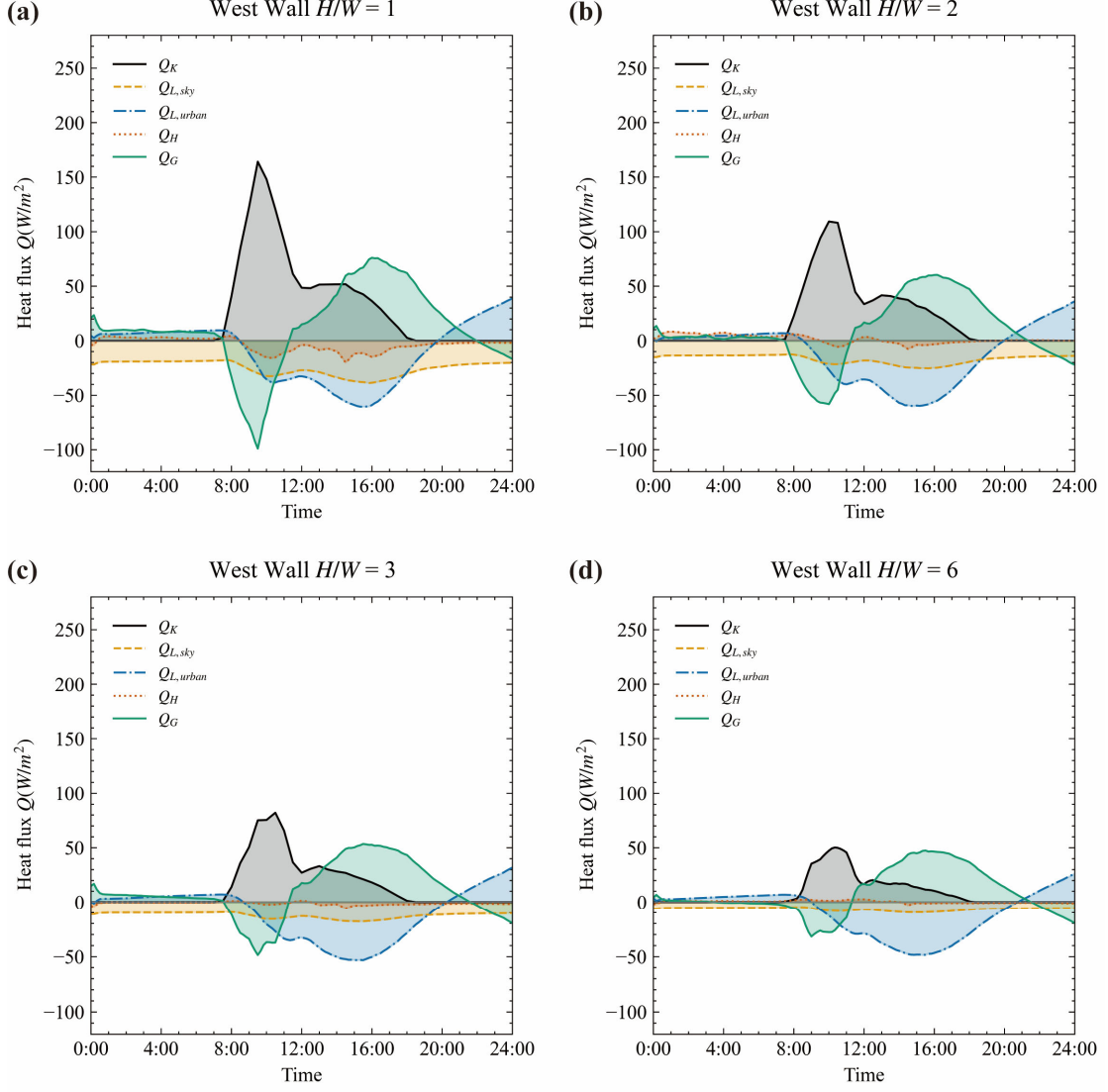
484 morning and positive in the afternoon, meaning that heat is stored in the building block during the
485 morning and released in the afternoon. In the reduced scale experiment, buildings were represented by
486 airtight hollow concrete blocks. Due to the lack of ventilation, the indoor air temperature can rise to 40°
487 C under an outdoor air temperature of 20°C, as shown in Appendix A. This indicates that the indoor air
488 can also absorb, store, and release a considerable amount of heat. Therefore, accurately modeling indoor
489 air temperature is essential for effective surface temperature modeling.

490 The convective heat flux contributes a smaller amount of the total heat flux. In high aspect ratio cases
491 ($H/W = 3$ and 6), the convective heat fluxes are almost negligible. This is due to the weak wind in the
492 deep street canyons. In this model, the surface convective heat flux is directly calculated from the wind
493 speeds in street canyons. This assumption may underestimate the convective flux, especially since natural
494 convection occurs under weak wind conditions ([Fan et al., 2021](#)).



495

496 **Figure 12: Diurnal heat fluxes at the east side walls from the simulation. The heat fluxes of solar (Q_K),**
 497 **longwave radiation (Q_L), convection (Q_H), and conduction (Q_G) are at the outer surface of walls.**



498

499 **Figure 13: Diurnal heat fluxes at the west side walls from the simulation. The heat fluxes of solar (Q_K),**
500 **longwave radiation (Q_L), convection (Q_H), and conduction (Q_G) are at the outer surface of walls.**

501 **4. Application to real urban configuration**

502 To demonstrate the model's applicability to complex geometries, we simulated a neighborhood
503 containing 40 buildings within an area of $350 \text{ m} \times 200 \text{ m}$. Building geometries were imported as STL
504 files comprising approximately 2.3×10^4 triangular surface meshes. Surface temperatures were calculated
505 on the triangular surface elements, as shown in Fig. 6, with shortwave fluxes resolved by a Monte Carlo
506 ray-tracing scheme using 1×10^5 photons. The solar position is updated at 30-min intervals to capture both
507 diurnal and shading variations. Transient heat conduction simulations were performed for 24 h with a

508 10-min time step (600 s) on 29 January 2021, consistent with the validation case. Downward solar
509 radiation, longwave radiation, wind speed, and air temperature were prescribed from the SOMUCH
510 measurements.

511 The simulation ran on a local workstation with an NVIDIA RTX 5090D GPU and completed in 26.6 h,
512 comprising a view-factor calculation (4.2 h), solar-radiation computation (22.2 h), and coupled heat-
513 transfer analysis (0.2 h).

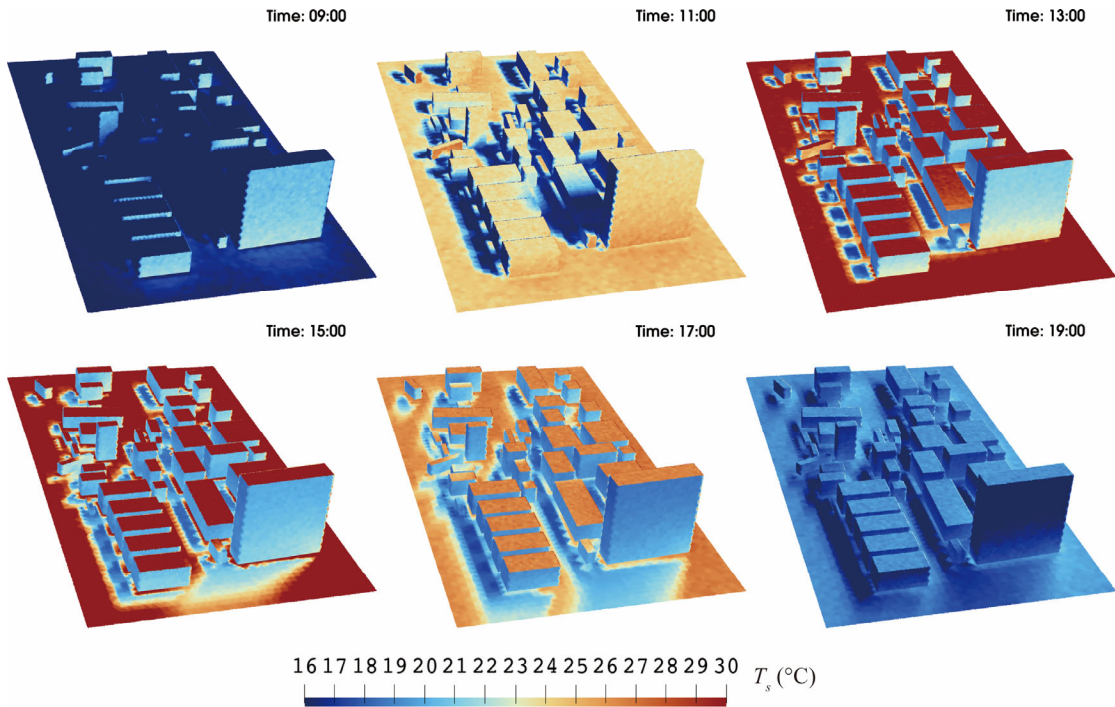
514 For this demonstration, material-specific reflectance was neglected and a uniform albedo of 0.24 was
515 applied to all urban surfaces. Walls and roofs were modeled as three concrete layers of 0.10 m each (total
516 thickness = 0.30 m), while the ground comprised 0.35 m (0.15 m + 0.15 m + 0.05 m) with an adiabatic
517 bottom boundary. For all layers, thermal properties were fixed to concrete values of thermal conductivity
518 $k = 2.0 \text{ W m}^{-1}\text{K}^{-1}$, density $\rho = 2420 \text{ kg m}^{-3}$, and specific heat capacity $c_p = 618 \text{ J kg}^{-1}\text{K}^{-1}$. All
519 model inputs are consolidated into a single YAML configuration file, which specifies the simulation
520 parameters, weather forcing, geometry paths, surface albedo, and material thermal properties for easy
521 reproducibility. The buildings are assumed to be naturally ventilated, with the indoor and outdoor air
522 temperatures being the same. The thermal characteristics of concrete are assumed to be the same as in
523 the SOMUCH experiment.

524 The surface temperatures are calculated in three steps: 1) calculate the solar radiative flux of each point
525 by rMCRT; 2) calculate the view factors between the elements using rMCRT; 3) calculate the surface
526 temperatures using Monte Carlo random walking. All three steps are processed in parallel on GPU. The
527 weather data measured on 29th Jan 2021 during the SOMUCH experiment is used as the driving input.
528 The surface temperatures are calculated from 0:00 to 24:00, with a time step of 30 minutes.

529 The simulation results were exported in vtk format and visualized using ParaView. Fig. 14 presents the
530 surface temperature distributions at 09:00, 11:00, 13:00, 15:00, 17:00, and 19:00. The movement of
531 building shadows and their influence on surface temperatures are clearly visible in these contours,
532 illustrating the diurnal heating and cooling cycle. These visualizations demonstrate that the model can
533 represent complex building geometries and can be applied to real urban environments.

534 The energy balance analysis of the SOMUCH experiment indicates that convective heat transfer plays

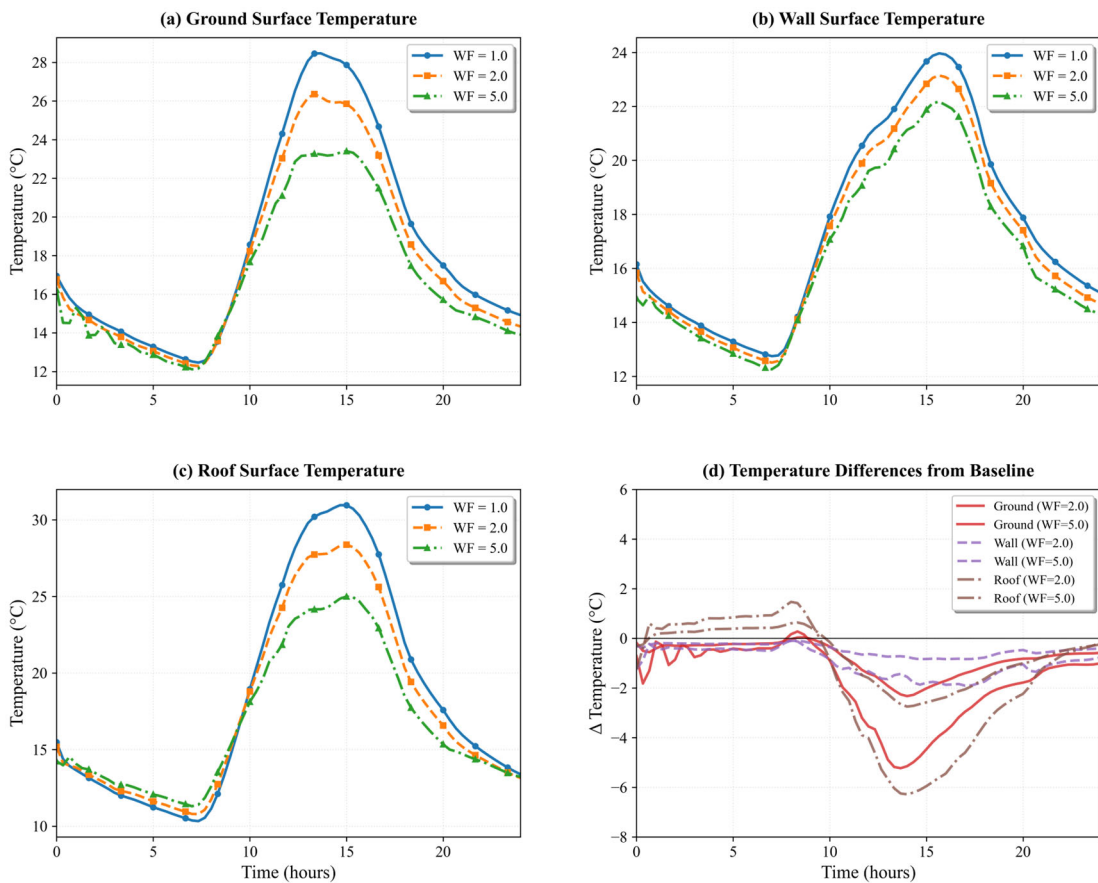
535 only a minor role. However, due to the experiment's reduced scale and limited local wind speeds, it
 536 remains uncertain whether this conclusion holds at full scale or under higher wind speed conditions.



537
 538 **Figure 14: Simulation results show the evolution of surface temperature for the complex building geometries**
 539 **at 09:00, 11:00, 13:00, 15:00, 17:00, and 19:00. These snapshots capture the diurnal heating and cooling cycle,**
 540 **highlighting morning warming, peak midday temperatures, and the evening decline.**

541 To further assess the role of the convective model, a wind sensitivity analysis was performed for the real
 542 urban configuration. The baseline wind speed ($WF = 1.0$) was measured on 29 January 2021, the same
 543 day used for the validation cases. Wind speeds were then systematically increased by factors of 2.0 and
 544 5.0 relative to the baseline to evaluate their influence on urban surface temperatures. The resulting
 545 average surface temperatures of the ground, walls, and roof are shown on Fig. 15. The temperature
 546 evolution in Fig. 15 (a)–(c) demonstrates that increasing the wind factor from $WF = 1.0$ to 5.0
 547 progressively lowers surface temperatures across all urban elements. Fig. 15 (d) quantifies the
 548 temperature differences relative to the baseline scenario ($WF = 1.0$), revealing cooling effects of up to
 549 6 °C, with the most pronounced reductions occurring during peak heating hours. Among the three
 550 surfaces, the roof exhibits the greatest sensitivity to wind variations, followed by the ground and then the
 551 walls.

552 These results highlight that, at full scale and under high-wind conditions, convective processes can exert
 553 a much stronger influence on urban surface temperatures than indicated by the scaled SOMUCH
 554 experiment. Therefore, future studies are needed to better quantify and model convective effects across
 555 a broader range of wind speeds and length scales. Moreover, under weak-wind conditions, natural
 556 convection becomes especially important, particularly when the temperature difference between the wall
 557 and the atmosphere grows large (Fan et al., 2021; Mei and Yuan, 2021). However, this natural-convective
 558 effect may not be significant in the scaled SOMUCH experiment.



559
 560 **Figure 15. Wind-sensitivity analysis of urban surface temperatures showing (a) ground, (b) wall, and (c) roof**
 561 **temperature evolution under different wind factors (WF = 1.0, 2.0, 5.0), and (d) temperature differences**
 562 **relative to the baseline (WF = 1.0). The baseline wind speed was measured on 29 January 2021, the same day**
 563 **used for the model-validation cases.**

564 **5. Limitations and future work**

565 This model is a building-resolved urban surface temperature model, focusing on detailed neighborhood-
566 scale processes. Therefore, its application to full city-scale simulations remains limited by computational
567 cost and is currently best suited for neighborhood-scale. The first version focuses on the complex
568 radiative exchange in densely built urban areas. The parameters and assumptions are validated against
569 the idealized scaled outdoor experiment, which uses homogeneous building materials with consistent
570 albedo and thermal characteristics. Glazing and green infrastructure are not included in this experiment.
571 The SOMUCH project is currently measuring the impact of glass and green infrastructure. The next
572 version will expand its capabilities to capture complex urban materials, such as urban trees, green walls,
573 and glass curtain walls, to better represent real urban configurations. Other limitations include:

- 574 • All reflections are assumed to be Lambertian. While this assumption works well for the SOMUCH
575 measurements, where concrete is used for all urban surfaces, it may not fully capture the reflective
576 properties of other materials with different surface textures, such as glass or vegetation.
- 577 • The high-resolution wall temperature simulation still requires a significant amount of time to
578 complete, even with parallel computation on GPUs. This is due to the large number of rays ($N =$
579 10^6) required for accurate solar radiation modeling. For each point, the simulation takes about 1
580 second to finish. However, as the number of test points increases, the overall computational time
581 grows substantially.
- 582 • The dynamic indoor air temperature is not included in this model. It assumes that the indoor air
583 temperature is equal to the outdoor air temperature for a natural ventilated room. This assumption
584 may lead to discrepancies, particularly in situations where indoor temperatures differ from outdoor
585 conditions due to factors such as heat sources, insulation, or limited ventilation.
- 586 • The participation of the urban atmosphere is ignored in this study. In the scaled measurements,
587 longwave radiation travels much shorter distances to adjacent surfaces, which reduces the influence
588 of atmospheric effects compared to real-world urban environments.
- 589 • Although many additional features will be incorporated into the GUST model in future
590 developments, this does not imply that the current version lacks applicability to real-world scenarios.

591 First, by focusing on the coupled radiative–convective–conductive heat transfer processes, GUST
592 effectively identifies the key physical mechanisms responsible for high urban surface temperatures.
593 Second, it provides high-quality building surface temperature predictions, which can be directly utilized
594 for building energy consumption analyses. Third, the inclusion of longwave radiative exchange between
595 urban surfaces enables GUST to be applied in the parameterization of longwave heat fluxes within
596 mesoscale urban climate models.

597 **6. Conclusions**

598 This study introduces a GPU-accelerated Urban Surface Temperature model (GUST), which computes
599 radiation using Monte Carlo ray tracing and solves heat conduction with a one-dimensional Monte Carlo
600 random-walk approach. To meet the substantial computational demands of these Monte Carlo
601 simulations, the model employs GPU-based parallel computing for efficient processing. GUST is
602 validated against the high-resolution, scaled outdoor experiment SOMUCH, which provides detailed
603 spatial and temporal measurements.

604 To accurately reproduce multiple reflections in high-density urban areas, the radiative heat flux is
605 simulated using~~The radiative heat flux is simulated using~~ a reverse Monte Carlo Ray Tracing method,
606 ~~which allows for the accurate reproduction of multiple reflections in high-density urban areas. Sensitivity~~
607 ~~tests~~The sensitivity test shows that $10^5 \sim 10^6$ rays are required for each point to accurately model the
608 solar radiation. This large computational demand for ray tracing is addressed using GPU-based parallel
609 computing.~~This large amount of ray tracing can only be achieved using GPU parallel computing. In~~
610 addition, the GPU is utilized to parallelize both the transient heat conduction, which is solved through
611 random-walk algorithms, and the longwave radiative exchange, which is also computed via ray tracing.
612 This integrated GPU-accelerated framework substantially improves the computational efficiency and
613 scalability of the GUST model.~~The Monte Carlo method is also used to solve the couple heat transfer~~
614 ~~using random walking algorithms, which is suitable for GPU based coding.~~

615 The comparison with the SOMUCH experiment shows that the transient surface temperatures on roofs,
616 walls and the ground are well reproduced. This comprehensive validation demonstrates the model's
617 ability to accurately capture the fine-scale radiative–convective–conductive heat transfer processes

618 within complex urban configurations. –By conducting a surface energy balance analysis, this study
619 demonstrates that longwave radiative exchange between urban surfaces plays a critical role across all
620 building density levels. In contrast, convective heat flux becomes significant only in high-density
621 configurations. A relatively large discrepancy is observed in cases with high building density, where the
622 wall temperatures are highly sensitive to convective and longwave radiative fluxes. The surface energy
623 balance analysis shows that longwave radiation exchange between urban surfaces plays a critical role
624 across all building densities. In contrast, convective heat flux only plays a significant role in high-density
625 cases. In future versions, the simulation of convective heat flux could be improved by simulating urban
626 airflow.

627 Lastly, this model is implemented to solve the surface temperatures on complex urban buildings, which
628 are composed of a total of 2.3×10^4 surface elements. The GPU allows simultaneous simulation of
629 heat transfer and view factors across all elements, enabling high-fidelity simulations in real urban
630 configurations with complex geometries. The current version focuses on the radiation-conduction-
631 convection coupled heat transfer coupled in complex geometries. Future developments will prioritize the
632 integration of complex glazing systems and green infrastructure in urban environments.

633

634 **Code availability**

635 The SOMUCH measurement data are available upon request. The development of GUST, model
636 validation, and visualization in this study were conducted using Python 3.8 with CUDA. The source code,
637 supporting data, and simulation results presented in this paper are archived on Zenodo ([Mei, 2025](#)) at
638 <https://doi.org/10.5281/zenodo.17138571> and are freely accessible for research purposes under the
639 Creative Commons Attribution 4.0 International (CC BY 4.0) license.

640

641 **Author contributions**

642 SM designed the study, developed the code, conducted the analysis. SM and GC prepared the manuscript
643 draft. GC and JH collected and shared SOMUCH measurements for the purpose of model validation. GC,

644 JH and TS supported the model implementation and data analysis. All have read and accepted the
645 manuscript for submission.

646

647 **Acknowledgement**

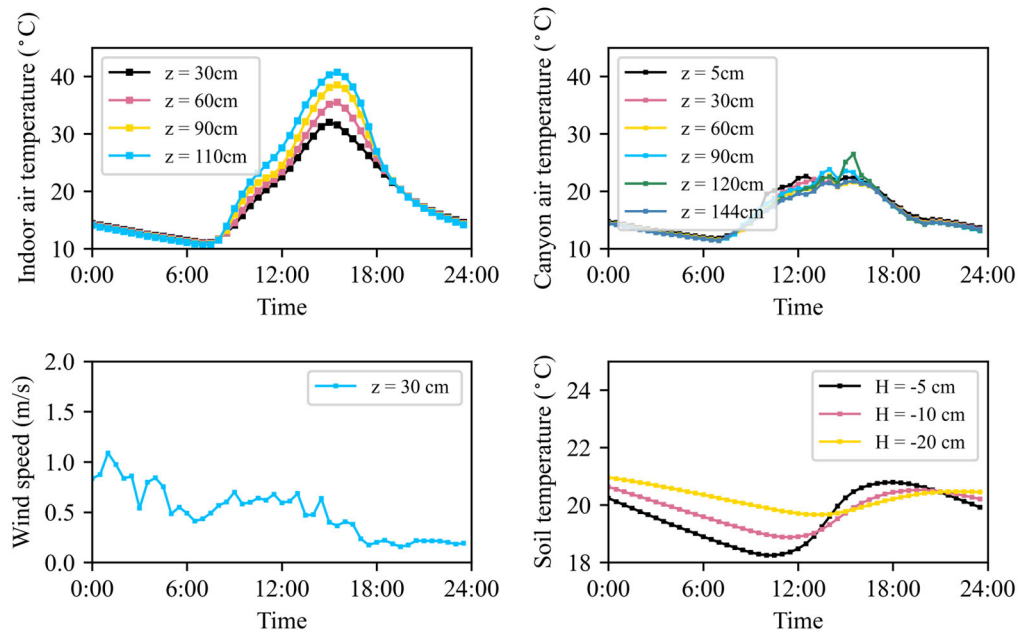
648 This research is supported by National Natural Science Foundation of China (Grant No. 42305076,
649 W2421048, U2442212), Natural Science Foundation of Guangdong Province, China (Grant No.
650 2024A1515010173) and Overseas Postdoctoral Talents 2023 Programme (Grant No. BH2023009). Dr.
651 Shuo-Jun Mei and Dr. Ting Sun are supported by an International Exchanges grant from the Royal
652 Society (Grant No. IEC\NSFC\242040) and National Natural Science Foundation of China (Grant No.
653 W2421048).

654

655 **Appendix A. Indoor and outdoor air temperatures in SOMUCH measurement**

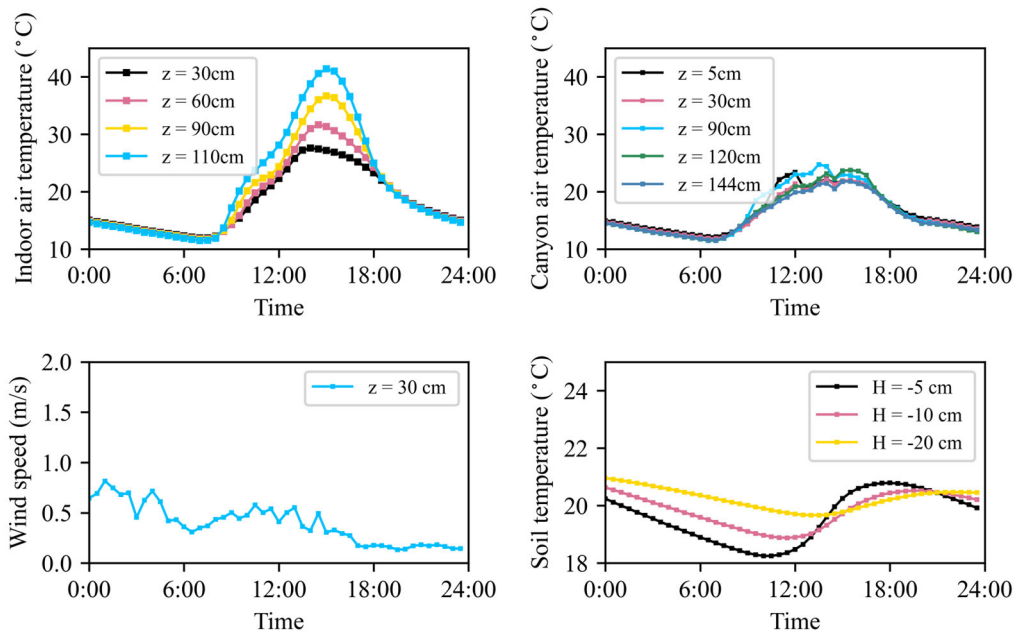
656 The indoor and outdoor air temperatures at different levels in the SOMUCH measurement are plotted in
657 Fig. A1. These air temperatures serve as input data for the validation cases.

(a) $H/W = 1$



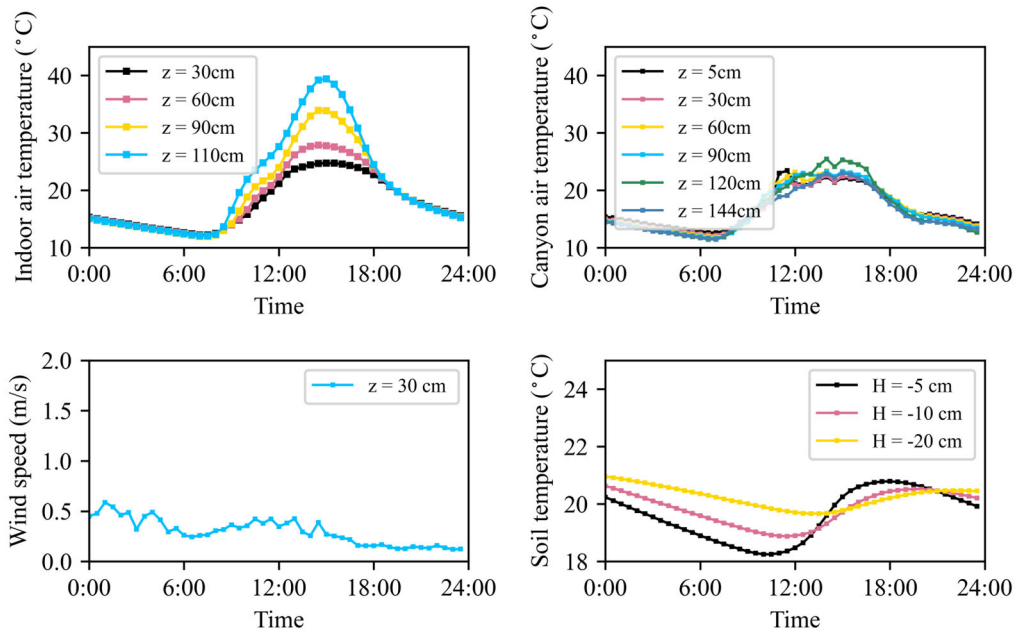
658

(b) $H/W = 2$



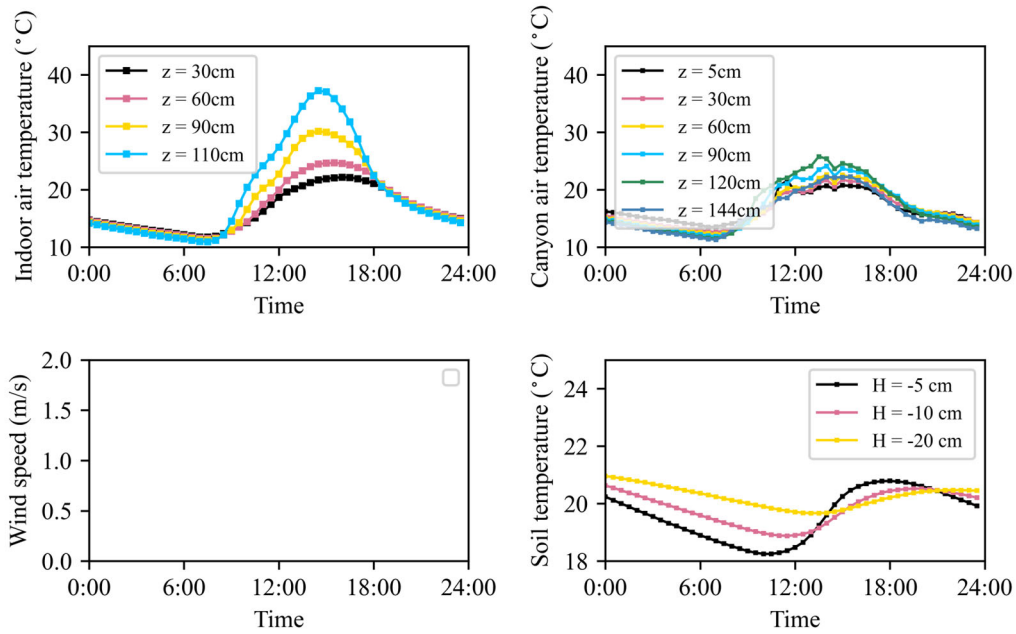
659

(c) $H/W = 3$



660

(d) $H/W = 6$



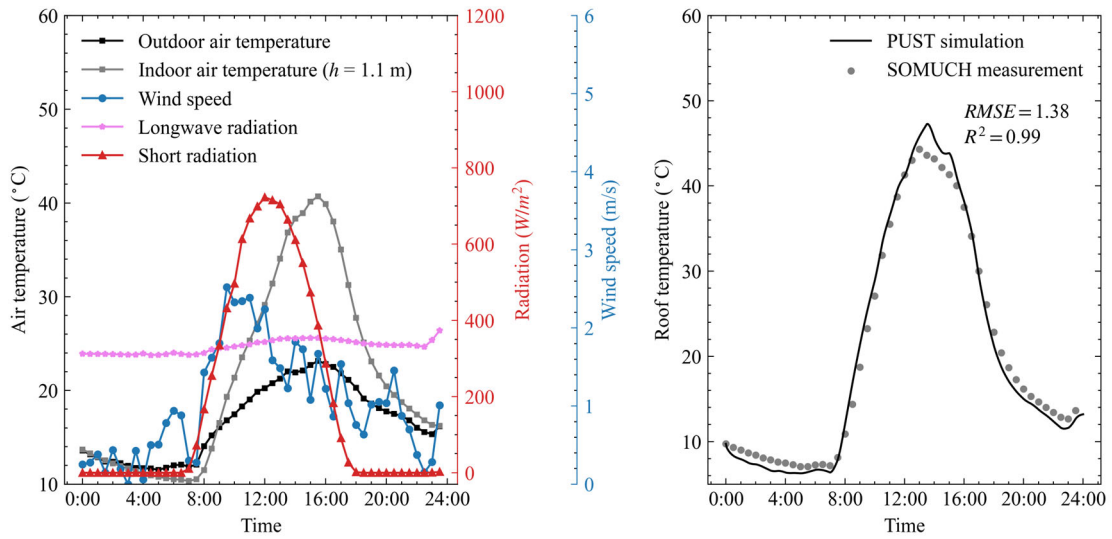
661

662 **Figure A1: Indoor, outdoor air temperatures, and wind speeds in street canyons that are measured on 29th**
663 **Jan 2021. The wind speeds in the street canyon of $H/W = 6$ were not measured because the sonic anemometer**
664 **cannot be installed in such a narrow street. The outdoor air temperatures measured at $z = 60$ cm in $H/W = 2$**
665 **are unusual, due to an instrument failure.**

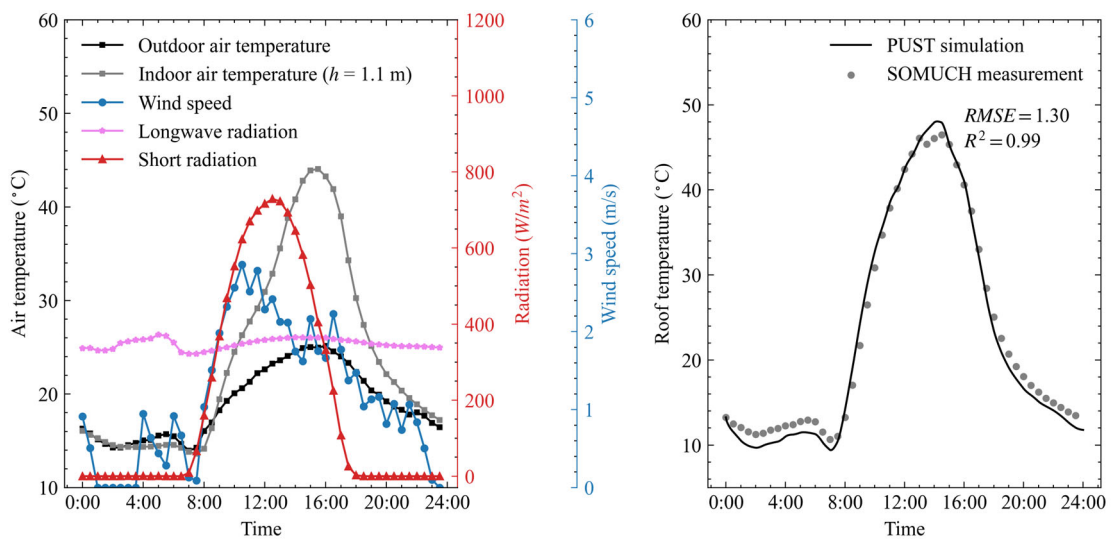
666 **Appendix B. Sensitivity test for other days**

667 To further validate the model, we also compared the simulated roof temperatures with measurements over three
668 consecutive days, from 30 January to 1 February 2021, similar to the analysis presented in Fig. 8. The results are
669 shown in Fig. A2, which demonstrates excellent agreement between simulated and observed roof temperatures. By
670 using multiple consecutive days, this comparison minimizes potential bias arising from the single day's weather
671 conditions.

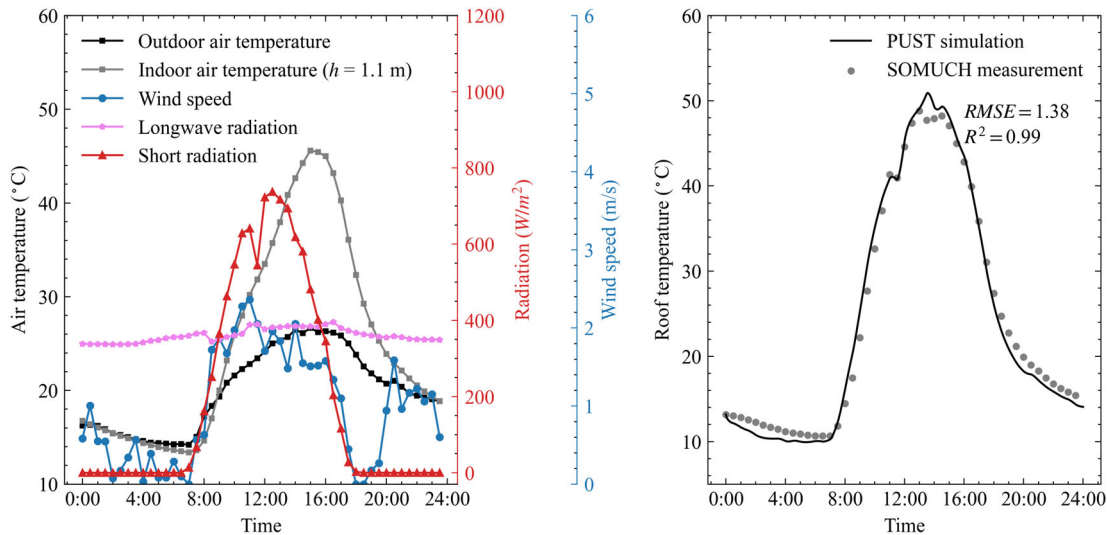
672 **(a) 30th Jan 2021**



674 (b) 31st Jan 2021



676 (c) 1st Feb 2021



677

678 **Figure A2: Weather data from 30 January to 1 February 2021 are shown in the left panels. The right panels**
 679 **compare roof-surface temperatures from simulation and measurement, with points representing observations**
 680 **and lines representing simulated values.**

681 References

682 Bentham, T. and Britter, R.: Spatially averaged flow within obstacle arrays, *Atmospheric Environment*,
 683 37, 2037-2043, [https://doi.org/10.1016/S1352-2310\(03\)00123-7](https://doi.org/10.1016/S1352-2310(03)00123-7), 2003.

684 Caliot, C., d'Alençon, L., Blanco, S., Forest, V., Fournier, R., Hourdin, F., Retailleau, F., Schoetter, R.,
 685 and Villefranque, N.: Coupled heat transfers resolution by Monte Carlo in urban geometry including
 686 direct and diffuse solar irradiations, *International Journal of Heat and Mass Transfer*, 222, 125139,
 687 <https://doi.org/10.1016/j.ijheatmasstransfer.2023.125139>, 2024.

688 Carmeliet, J. and Derome, D.: How to beat the heat in cities through urban climate modelling, *Nature*
 689 *Reviews Physics*, 6, 2-3, 10.1038/s42254-023-00673-1, 2024.

690 Chen, G., Mei, S.-J., Hang, J., Li, Q., and Wang, X.: URANS simulations of urban microclimates:
 691 Validated by scaled outdoor experiments, *Building and Environment*, 272, 112691,
 692 <https://doi.org/10.1016/j.buildenv.2025.112691>, 2025.

693 Ebi, K. L., Capon, A., Berry, P., Broderick, C., de Dear, R., Havenith, G., Honda, Y., Kovats, R. S., Ma,
 694 W., Malik, A., Morris, N. B., Nybo, L., Seneviratne, S. I., Vanos, J., and Jay, O.: Hot weather and
 695 heat extremes: health risks, *The Lancet*, 398, 698-708, [https://doi.org/10.1016/S0140-6736\(21\)01208-3](https://doi.org/10.1016/S0140-6736(21)01208-3), 2021.

697 Eingrüber, N., Domm, A. S., Korres, W., and Schneider, K.: Simulation of the heat mitigation potential
 698 of unsealing measures in cities by parameterizing grass grid pavers for urban microclimate modelling
 699 with ENVI-met (V5), *EGUphere*, 2024, 1-25, 10.5194/egusphere-2024-697, 2024.

700 Fan, Y., Zhao, Y., Torres, J. F., Xu, F., Lei, C., Li, Y., and Carmeliet, J.: Natural convection over vertical

701 and horizontal heated flat surfaces: A review of recent progress focusing on underpinnings and
702 implications for heat transfer and environmental applications, *Physics of Fluids*, 33, 101301,
703 10.1063/5.0065125, 2021.

704 Feng, J., Gao, K., Khan, H., Ulpiani, G., Vasilakopoulou, K., Young Yun, G., and Santamouris, M.:
705 Overheating of Cities: Magnitude, Characteristics, Impact, Mitigation and Adaptation, and Future
706 Challenges, *Annual Review of Environment and Resources*, 48, 651-679,
707 <https://doi.org/10.1146/annurev-environ-112321-093021>, 2023.

708 Forouzandeh, A.: Prediction of surface temperature of building surrounding envelopes using holistic
709 microclimate ENVI-met model, *Sustainable Cities and Society*, 70, 102878,
710 <https://doi.org/10.1016/j.scs.2021.102878>, 2021.

711 Grimmond, C. S. B. and Oke, T. R.: Aerodynamic properties of urban areas derived from analysis of
712 surface form, *Journal of Applied Meteorology*, 38, 1262, 10.1175/1520-
713 0450(1999)038<1262:APOUAD>2.0.CO;2, 1999.

714 Grimmond, C. S. B., Blackett, M., Best, M. J., Barlow, J., Baik, J.-J., Belcher, S. E., Bohnenstengel, S.
715 I., Calmet, I., Chen, F., Dandou, A., Fortuniak, K., Gouvea, M. L., Hamdi, R., Hendry, M., Kawai,
716 T., Kawamoto, Y., Kondo, H., Krayenhoff, E. S., Lee, S.-H., Lorida, T., Martilli, A., Masson, V.,
717 Miao, S., Oleson, K., Pigeon, G., Porson, A., Ryu, Y.-H., Salamanca, F., Shashua-Bar, L., Steeneveld,
718 G.-J., Tombrou, M., Voogt, J., Young, D., and Zhang, N.: The International Urban Energy Balance
719 Models Comparison Project: First Results from Phase 1, *Journal of Applied Meteorology and*
720 *Climatology*, 49, 1268-1292, <https://doi.org/10.1175/2010JAMC2354.1>, 2010.

721 Grimmond, C. S. B., Blackett, M., Best, M. J., Baik, J.-J., Belcher, S. E., Beringer, J., Bohnenstengel, S.
722 I., Calmet, I., Chen, F., Coutts, A., Dandou, A., Fortuniak, K., Gouvea, M. L., Hamdi, R., Hendry,
723 M., Kanda, M., Kawai, T., Kawamoto, Y., Kondo, H., Krayenhoff, E. S., Lee, S.-H., Lorida, T.,
724 Martilli, A., Masson, V., Miao, S., Oleson, K., Ooka, R., Pigeon, G., Porson, A., Ryu, Y.-H.,
725 Salamanca, F., Steeneveld, G. J., Tombrou, M., Voogt, J. A., Young, D. T., and Zhang, N.: Initial
726 results from Phase 2 of the international urban energy balance model comparison, *International*
727 *Journal of Climatology*, 31, 244-272, <https://doi.org/10.1002/joc.2227>, 2011.

728 Hang, J. and Chen, G.: Experimental study of urban microclimate on scaled street canyons with various
729 aspect ratios, *Urban Climate*, 46, 101299, <https://doi.org/10.1016/j.uclim.2022.101299>, 2022.

730 Hang, J., Zeng, L., Li, X., and Wang, D.: Evaluation of a single-layer urban energy balance model using
731 measured energy fluxes by scaled outdoor experiments in humid subtropical climate, *Building and*
732 *Environment*, 254, 111364, <https://doi.org/10.1016/j.buildenv.2024.111364>, 2024.

733 Hang, J., Lu, M., Ren, L., Dong, H., Zhao, Y., and Zhao, N.: Cooling performance of near-infrared and
734 traditional high-reflective coatings under various coating modes and building area densities in 3D
735 urban models: Scaled outdoor experiments, *Sustainable Cities and Society*, 121, 106200,
736 <https://doi.org/10.1016/j.scs.2025.106200>, 2025.

737 Hénon, A., Mestayer, P. G., Lagourde, J.-P., and Voogt, J. A.: An urban neighborhood temperature and
738 energy study from the CAPITOUL experiment with the Solene model, *Theoretical and Applied*

739 Climatology, 110, 197-208, 10.1007/s00704-012-0616-z, 2012.

740 Imbert, C., Bhattacharjee, S., and Tencar, J.: Simulation of urban microclimate with SOLENE-
741 microclimat: an outdoor comfort case study, Proceedings of the Symposium on Simulation for
742 Architecture and Urban Design, Delft, Netherlands2018.

743 Kondo, A., Ueno, M., Kaga, A., and Yamaguchi, K.: The Influence Of Urban Canopy Configuration On
744 Urban Albedo, Boundary-Layer Meteorology, 100, 225-242, 10.1023/A:1019243326464, 2001.

745 Krayenhoff, E. S. and Voogt, J. A.: A microscale three-dimensional urban energy balance model for
746 studying surface temperatures, Boundary-Layer Meteorology, 123, 433-461, 10.1007/s10546-006-
747 9153-6, 2007.

748 Manoli, G., Fatichi, S., Schläpfer, M., Yu, K., Crowther, T. W., Meili, N., Burlando, P., Katul, G. G., and
749 Bou-Zeid, E.: Magnitude of urban heat islands largely explained by climate and population, Nature,
750 573, 55-60, 10.1038/s41586-019-1512-9, 2019.

751 Mei, S.-J.: GUST1.0: A GPU-accelerated 3D Urban Surface Temperature Model (1.1),
752 <https://doi.org/10.5281/zenodo.17138571>, 2025.

753 Mei, S.-J. and Yuan, C.: Three-dimensional simulation of building thermal plumes merging in calm
754 conditions: Turbulence model evaluation and turbulence structure analysis, Building and
755 Environment, 203, 108097, <https://doi.org/10.1016/j.buildenv.2021.108097>, 2021.

756 Mei, S.-J., Chen, G., Wang, K., and Hang, J.: Parameterizing urban canopy radiation transfer using three-
757 dimensional urban morphological parameters, Urban Climate, 60, 102363,
758 <https://doi.org/10.1016/j.uclim.2025.102363>, 2025.

759 Nice, K.: Development, validation, and demonstration of the VTUF-3D v1. 0 urban micro-climate model
760 to support assessments of urban vegetation influences on human thermal comfort, School of Earth,
761 Atmosphere and Environment, Monash University, 2016.

762 Owens, S. O., Majumdar, D., Wilson, C. E., Bartholomew, P., and van Reeuwijk, M.: A conservative
763 immersed boundary method for the multi-physics urban large-eddy simulation model uDALES v2.0,
764 Geoscientific Model Development, 17, 6277-6300, 10.5194/gmd-17-6277-2024, 2024.

765 Reindl, D. T., Beckman, W. A., and Duffie, J. A.: Diffuse fraction correlations, Solar Energy, 45, 1-7,
766 [https://doi.org/10.1016/0038-092X\(90\)90060-P](https://doi.org/10.1016/0038-092X(90)90060-P), 1990.

767 Resler, J., Krc, P., Belda, M., Jurus, P., Benesova, N., Lopata, J., Vlcek, O., Damaskova, D., Eben, K.,
768 Derbek, P., Maronga, B., and Kanani-Suhring, F.: PALM-USM v1.0: A new urban surface model
769 integrated into the PALM large-eddy simulation model, Geoscientific Model Development, 10, 3635-
770 3659, 10.5194/gmd-10-3635-2017, 2017.

771 Rodriguez, A., Lecigne, B., Wood, S., Carmeliet, J., Kubilay, A., and Derome, D.: Optimal representation
772 of tree foliage for local urban climate modeling, Sustainable Cities and Society, 115, 105857,
773 <https://doi.org/10.1016/j.scs.2024.105857>, 2024.

774 Salim, M. H., Schlünzen, K. H., Grawe, D., Boettcher, M., Gierisch, A. M. U., and Fock, B. H.: The

775 microscale obstacle-resolving meteorological model MITRAS v2.0: model theory, Geoscientific
776 Model Development, 11, 3427-3445, 10.5194/gmd-11-3427-2018, 2018.

777 Schoetter, R., Caliot, C., Chung, T.-Y., Hogan, R. J., and Masson, V.: Quantification of Uncertainties of
778 Radiative Transfer Calculation in Urban Canopy Models, Boundary-Layer Meteorology, 189, 103-
779 138, 10.1007/s10546-023-00827-9, 2023.

780 Talebi, S., Gharehbash, K., and Jalali, H. R.: Study on random walk and its application to solution of heat
781 conduction equation by Monte Carlo method, Progress in Nuclear Energy, 96, 18-35,
782 <https://doi.org/10.1016/j.pnucene.2016.12.004>, 2017.

783 Topalar, Y., Blocken, B., Vos, P., van Heijst, G. J. F., Janssen, W. D., van Hooff, T., Montazeri, H., and
784 Timmermans, H. J. P.: CFD simulation and validation of urban microclimate: A case study for
785 Bergpolder Zuid, Rotterdam, Building and Environment, 83, 79-90,
786 <https://doi.org/10.1016/j.buildenv.2014.08.004>, 2015.

787 Tregan, J. M., Amestoy, J. L., Bati, M., Bezian, J.-J., Blanco, S., Brunel, L., Caliot, C., Charon, J., Cornet,
788 J.-F., Coustet, C., d'Alençon, L., Dauchet, J., Dutour, S., Eibner, S., El Hafi, M., Eymet, V., Farges,
789 O., Forest, V., Fournier, R., Galtier, M., Gattepaille, V., Gautrais, J., He, Z., Hourdin, F., Ibarrat, L.,
790 Joly, J.-L., Lapeyre, P., Lavieille, P., Lecureux, M.-H., Lluc, J., Miscevic, M., Mourtaday, N.,
791 Nyffenegger-Péré, Y., Pelissier, L., Penazzi, L., Piaud, B., Rodrigues-Viguier, C., Roques, G., Roger,
792 M., Saez, T., Terrée, G., Villefranque, N., Vourc'h, T., and Yaacoub, D.: Coupling radiative,
793 conductive and convective heat-transfers in a single Monte Carlo algorithm: A general theoretical
794 framework for linear situations, PLoS One, 18, e0283681, 10.1371/journal.pone.0283681, 2023.

795 Tuholske, C., Caylor, K., Funk, C., Verdin, A., Sweeney, S., Grace, K., Peterson, P., and Evans, T.: Global
796 urban population exposure to extreme heat, Proceedings of the National Academy of Sciences of the
797 United States of America, 118, e2024792118, doi:10.1073/pnas.2024792118, 2021.

798 Villefranque, N., Hourdin, F., d'Alençon, L., Blanco, S., Boucher, O., Caliot, C., Coustet, C., Dauchet,
799 J., El Hafi, M., Eymet, V., Farges, O., Forest, V., Fournier, R., Gautrais, J., Masson, V., Piaud, B., and
800 Schoetter, R.: The “teapot in a city”: A paradigm shift in urban climate modeling, Science Advances,
801 8, eabp8934, doi:10.1126/sciadv.abp8934, 2022.

802 Voogt, J. A. and Oke, T. R.: Effects of urban surface geometry on remotely-sensed surface temperature,
803 International Journal of Remote Sensing, 19, 895-920, 10.1080/014311698215784, 1998.

804 Wang, K., Li, Y., Li, Y., and Lin, B.: Stone forest as a small-scale field model for the study of urban
805 climate, International Journal of Climatology, 38, 3723-3731, <https://doi.org/10.1002/joc.5536>, 2018.

806 Wang, W., Wang, X., and Ng, E.: The coupled effect of mechanical and thermal conditions on pedestrian-
807 level ventilation in high-rise urban scenarios, Building and Environment, 191, 107586,
808 <https://doi.org/10.1016/j.buildenv.2021.107586>, 2021.

809 Wu, Z., Shi, Y., Ren, L., and Hang, J.: Scaled outdoor experiments to assess impacts of tree
810 evapotranspiration and shading on microclimates and energy fluxes in 2D street canyons, Sustainable
811 Cities and Society, 108, 105486, <https://doi.org/10.1016/j.scs.2024.105486>, 2024.

812 Yang, X. and Li, Y.: Development of a Three-Dimensional Urban Energy Model for Predicting and
813 Understanding Surface Temperature Distribution, *Boundary-Layer Meteorology*, 149, 303-321,
814 10.1007/s10546-013-9842-x, 2013.

815 Yang, X. and Li, Y.: The impact of building density and building height heterogeneity on average urban
816 albedo and street surface temperature, *Building and Environment*, 90, 146-156,
817 <https://doi.org/10.1016/j.buildenv.2015.03.037>, 2015.

818 Yoshida, K., Miwa, S., Yamaki, H., and Honda, H.: Analyzing the impact of CUDA versions on GPU
819 applications, *Parallel Computing*, 120, 103081, <https://doi.org/10.1016/j.parco.2024.103081>, 2024.

820 Yuan, C., Adelia, A. S., Mei, S., He, W., Li, X.-X., and Norford, L.: Mitigating intensity of urban heat
821 island by better understanding on urban morphology and anthropogenic heat dispersion, *Building*
822 and *Environment*, 176, 106876, <https://doi.org/10.1016/j.buildenv.2020.106876>, 2020.

823 Yuan, C., Shan, R., Zhang, Y., Li, X.-X., Yin, T., Hang, J., and Norford, L.: Multilayer urban canopy
824 modelling and mapping for traffic pollutant dispersion at high density urban areas, *Science of The*
825 *Total Environment*, 647, 255-267, <https://doi.org/10.1016/j.scitotenv.2018.07.409>, 2019.

826